



LIETUVOS
ENERGETIKOS
INSTITUTAS



Vilnius University
Institute of
Theoretical Physics
and Astronomy

Annual Report of the Association EURATOM / LEI

2012

ISSN 2029-1612 (print)

ISSN 2351-6976 (online)

© Lithuanian Energy Institute, 2013

Content

Executive summary.....	4
General information	6
1 Assessment of Plasma Vessel venting system capacity	7
1.1 Description of W7-X Plasma Vessel venting system.....	7
1.2 Description of the model for COCOSYS.....	8
1.3 Results of analysis	9
1.3.1 The base case scenario	10
1.3.2 Comparison with RELAP5 results	12
1.4 Summary of PV venting system assessment	14
2 Limit Analysis of the Port Welds between the Plasma Vessel and the Ports in the W7-X Cryostat System	16
2.1 Models and boundary conditions.....	16
2.2 Results of limit load analysis	20
2.2.1 Results of Port AEU30 with a 1 mm gap.....	20
2.2.2 Results of Port AEU30 6 mm gap	24
2.3 Summary of limit load analysis.....	29
3 W7-X probabilistic risk analysis.....	31
4 Theoretical investigations for plasma diagnostics.....	35
4.1 Investigation of spectroscopic parameters of tungsten ions.....	36
4.2 New method for evaluation of the accuracy of electron transitions	38
4.3 Theoretical calculation of dielectronic recombination coefficients for fusion plasma in relativistic approximation	45
4.4 Investigation of energy spectrum and decay probabilities in Cs atom and Cs ⁻ ion	46
4.5 References for Chapter 4	50
5 Mobility program 2012	51
6 Other activities in magnetic confinement fusion.....	53
7 Public information.....	54
8 Publications	55

EXECUTIVE SUMMARY

Lithuanian Energy Institute (LEI) signed a contract on joining the European Fusion Development Agreement (EFDA) and starting from the 1st of January, 2007 Lithuania officially became a EFDA member. In 2012 EURATOM/LEI association successfully continued activities in research related to European Fusion Development Agreement activities. Our activities concentrate around three issues: Fusion safety issues, Plasma diagnostics and Technology development for burning plasmas.

The largest part of our activities is related to Wendelstein 7-X programme implemented by Max-Planck-Institut für Plasmaphysik (IPP) in Germany. In 2012 our association performed the assessment of the water hammer effect during normal operation and a detailed assessment of W7-X Plasma Vessel venting system capacity, the limit load analysis of the port welds, the assessment of the pipe whip possibility in case of pipe rupture as well as the assessment of cooling circuit in case of loss of off-site power.

The assessment of W7-X Plasma Vessel venting system capacity was performed using computer codes RELAP5 and COCOSYS. RELAP5 was used to determine the mass and energy flow rates through the ruptured pipe and gas flows through the venting system. A detailed thermal-hydraulic model was developed to represent the complicated cooling system of W7-X. COCOSYS code was used for a detailed analysis of Plasma Vessel venting system. Different scenarios were investigated to estimate the acceptance of the design of the venting system. The performed analysis showed that the current design of Plasma Vessel venting system ensures pressures below design limits.

The port welds between the Plasma Vessel and the ports in W7-X cryostat system was investigated and analysis was performed to define the limit load for welding connection between the port AEU30 and the PV shell with a 1 mm and 6 mm gap. The welding efficiency for analysis was assumed 0.7 and 0.85. The received results showed that limit loads are significantly higher than expected loads during operation, thus the integrity of the welding will be ensured.

Probabilistic analysis of freezing of W7-X water cooling circuit ABK10, which is located close to the cold cryostat, in case of loss of offsite power supply was performed. Several accident scenarios that could lead to circuit freezing were investigated: 1) failure of Emergency Diesel Generator and switch to alternative power source, 2) failure to restart circulation and 3) failure to drain water. The results show rather high safety barrier against the initiating event; however, several recommendations were given to increase reliability of the system.

In 2012 the first JET Notification of Lithuanian Energy Institute was signed to perform calculations of dose rates from shields in support of JET neutron detector calibration. MCNP code was used for the analysis. The results were discussed during semiannual monitoring meetings at CCFE (Culham, UK). At present, the final report is being finalised after the comments, raised during the meeting in Culham in December 2012.

Tungsten as a heat-resistant material is planned to be used at ITER. Using tungsten in some parts of the tokamak may solve the tritium retention problem. On the other hand, tungsten atoms can detach from the inner walls of the fusion reactor, penetrate into the plasma and be ionised to very high degrees. Various tungsten ions will irradiate strongly thus cooling the plasma. Our association performed theoretical studies of the spectroscopic characteristics of highly charged tungsten atoms

having open d and f-shells accounting for relativistic and correlation effects. These results could contribute to development of plasma diagnostic techniques in the future.

In 2012 the total research volume of the 2012 activities was ~7 professional man-years. Details on all the performed activities are given in further sections of this report.

GENERAL INFORMATION

EURATOM/LEI Steering Committee

European Commission

Mr. Simon Webster, Head of Unit – K6 (Fusion Association Agreements) SC member from September 2012

Mr. Vito Marchese, Scientific Officer RTD – K6 (Fusion Association Agreements)

Mr. Ruggero Giannella, Scientific Officer RTD – K6 (Fusion Association Agreements) in September 2012 replaced by Ms. Rosa Antidormi, Scientific Officer RTD – K6 (Fusion Association Agreements) and acting as alternating member

Mr. Marc Cosyns, Administrator RTD – K7 (Administration and Finances)

Lithuania

Mr. Romualdas Kisielius (Vilnius University Institute of Theoretical Physics and Astronomy)

Mr. Liudvikas Pranevičius, Vytautas Magnus University

Mr. Stanislovas Žurauskas, Ministry of Education and Science

EURATOM/LEI Head of Research Unit

Eugenijus Ušpuras

Lithuanian Energy Institute

Breslaujos g. 3, LT-44403 Kaunas, Lithuania

Phone: +370 37 401926

Fax: +370 37 351271

e-mail: uspuras@mail.lei.lt

Research Unit in Lithuania

Lithuanian Energy Institute

Breslaujos g. 3, LT-44403 Kaunas, Lithuania

Phone: +370 37 401801

Fax: +370 37 351271

e-mail: rastine@mail.lei.lt

URL: <http://www.lei.lt>

Vilnius University Institute of Theoretical Physics and Astronomy

A. Goštauto g. 12, LT-01108 Vilnius, Lithuania,

Phone: +370 5 2193251,

Fax: +370 5 2125361,

e-mail: tfai@tfai.vu.lt

URL: <http://www.tfai.vu.lt/>

1 ASSESSMENT OF PLASMA VESSEL VENTING SYSTEM CAPACITY

The principal investigators for this task are E. Urbonavičius and T. Kaliatka of LEI.

To protect the Plasma Vessel from overpressure in case of loss of coolant accident the venting system is installed, which consists of two burst disks and associated piping to direct the released steam from Plasma Vessel to environment. The analysis was performed to investigate whether the piping and condensation of steam imposes additional resistance, which could potentially lead to higher pressure in Plasma Vessel. For the analysis, 40 mm diameter pipe rupture inside Plasma Vessel during “baking” mode was assumed.

The report includes a short description of the venting system, a description of the developed model for COCOSYS code, and results of the performed calculations. The COCOSYS code results are also compared to the results received using RELAP5 code, which was also used to calculate the water discharge from the ruptured pipe of the Plasma Vessel cooling circuit. At the end of the report, conclusions of the performed analysis are formulated.

1.1 Description of W7-X Plasma Vessel venting system

The layout of piping of W7-X Plasma Vessel venting system is shown in Figure 1.1. To protect the Plasma Vessel from overpressure two burst disks are installed: 1) one with opening pressure of 1.1 bar and 2) one with opening pressure of 1.2 bar. Diameter of both burst disks is 250 mm. Both burst disks are installed on the pipelines of 300 mm inner diameter that are connected to the main pipeline of 500 mm inner diameter. The exit of the main pipeline is outside the building above the roof level.

In case of a loss of coolant accident inside the plasma vessel, the opening pressure of the burst disk would be reached and after disk opening steam would enter piping of the venting system and would be directed outside the building. The steam would be condensing on the colder surfaces of

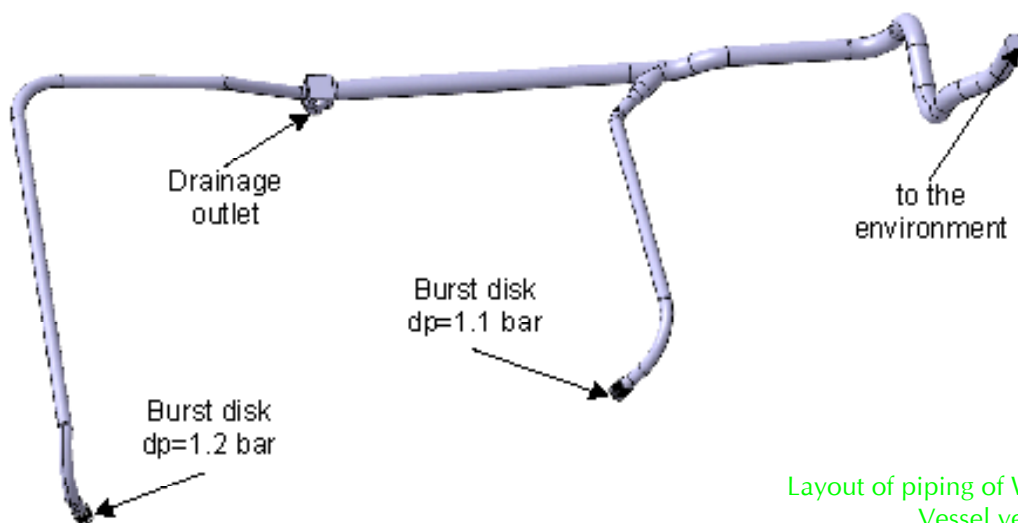


Figure 1.1
Layout of piping of W7-X Plasma Vessel venting system

the piping; therefore, the piping is designed with an inclination, which ensures that water flows to the drainage outlet.

1.2 Description of the model for COCOSYS

The nodalisation scheme of W7-X Plasma Vessel venting system is presented in Figure 1.2. The volume of each node and the associated areas of the structures connected to the nodes are presented as well. The red lines show junctions between the nodes for atmospheric flow, and the blue arrows indicate the flow of water, which appears due to steam condensation. Node LEIT1 represents the shorter line with the burst disk of 1.1 bar opening pressure. Node LEIT2 represents the longer line with a burst disk of opening pressure of 1.2 bar. Also, this node includes a part of the main line with the drainage outlet. Both node LEIT1 and LEIT2 are connected to node GABEL, which represents the “fork” of the connected pipes. The rest part of the main pipeline inside the building is represented by the node HAUPT. In the model, it is assumed that a certain part of the pipe would be located outside the building, and this part is represented by node CHIMNEY. The volume of the nodes was calculated from the drawings provided by W7-X team.

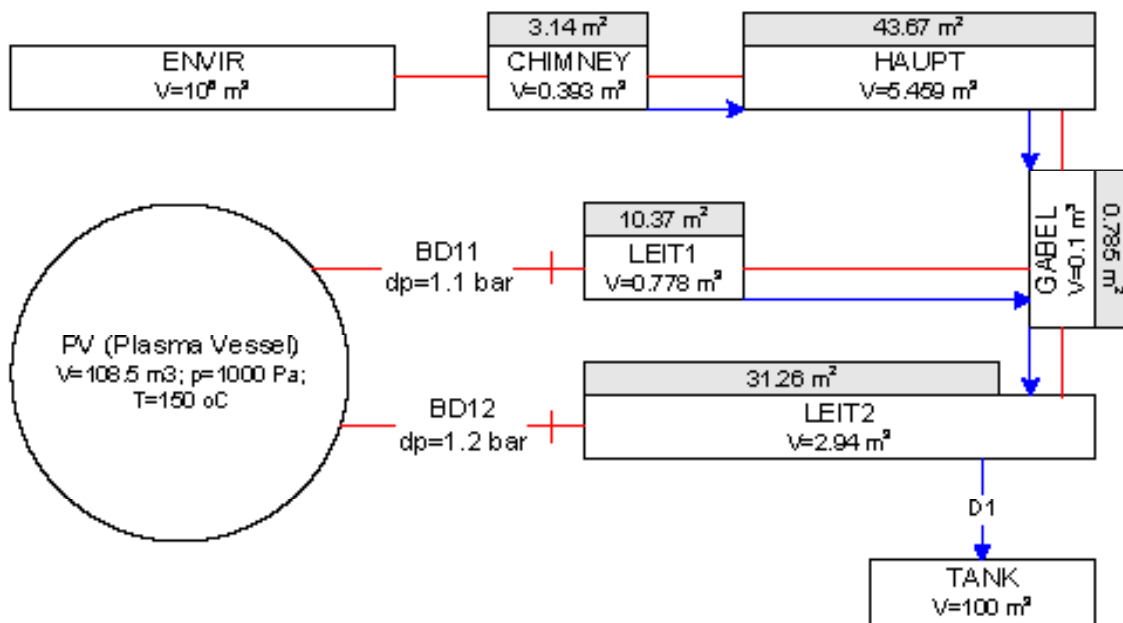


Figure 1.2
Nodalisation scheme of W7-X venting system for COCOSYS

The gas temperature inside the building was assumed 20 °C with the relative humidity of 60 %. The same temperature and humidity was assumed inside the piping of the venting system. The initial temperature (before the accident) inside the plasma vessel is 150 °C.

In COCOSYS code the atmospheric and water flows are simulated separately; therefore, separate junctions have to be defined. The rupture disks are simulated by a special junction type, which considers that after reaching a defined set point, the junction opens and stays open until the end of the analysis. The other atmospheric junctions are always open. The associated flow loss coefficients were estimated taking into account friction loss and local pressure losses due to changing flow

direction and diameter. In the model it is assumed that the water starts flowing from one node to another when the water film thickness on the inner surface of the pipe reaches 1 mm.

The piping is made of stainless steel of 1 mm thickness. The heat transfer area of the piping was calculated from the drawings provided by W7-X team. It is assumed that heat exchange on both surfaces could occur due to convection, condensation and wall to gas radiation.

The outer surface of structure associated with this node faces the outside environment, which could have temperature that is different from the temperature inside the building. For the base case analysis, it was assumed that the temperature in the outside environment is also 20 °C.

The structures of the plasma vessel were assumed to be hot with temperature of 150 °C. Such temperature is constant during the entire calculation time. Since COCOSYS code cannot simulate deep vacuum conditions, it is assumed that the initial pressure inside the plasma vessel is 1000 Pa, which is the lowest possible pressure possible in the code.

The analysis of the venting system was performed for the loss of coolant accident scenario, which assumes 40 mm diameter pipe rupture in the operation mode “Baking”. During this operation mode, the inner surfaces in the plasma vessel are cleaned from impurities and plasma vessel is prepared for plasma ignition. The coolant release rate and the specific enthalpy of the released coolant were calculated using RELAP5 code and are shown in Figure 1.3. After the pipe rupture, the maximal flow rate through the break into the plasma vessel reaches ~28 kg/s, but after this peak it gradually decreases. This decrease is related to closure of the automatic valves in the baking circuit. After 25 s, the release rate to the plasma vessel is ~5 kg/s, and after 80 s it is <2 kg/s. The specific enthalpy of the released coolant changes with the time – at first only water is released, but after ~75 s, the superheated steam appears.

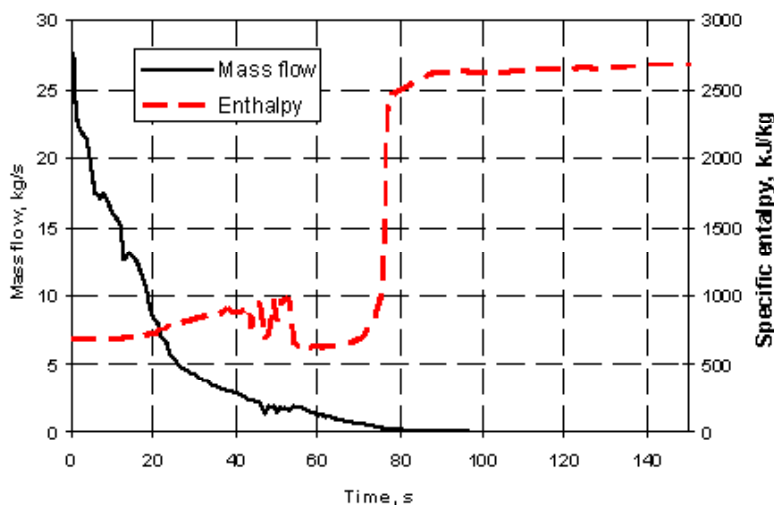


Figure 1.3
Coolant release rate and specific enthalpy to plasma vessel received from RELAP5 code analysis

1.3 Results of analysis

To investigate the piping of venting system in case of LOCA during “baking” mode, the following variants were investigated:

1. The base case scenario when the entire system operates as expected;
2. Base case comparison with RELAP5 results;
3. Failure of burst disk opening at 1.1 bar;

4. Temperature of outside environment 0 °C;
5. Influence of coolant release rate;
6. Influence of pressure losses inside venting system pipes.

In this report details will be described only for 1 and 2 investigated variants.

1.3.1 The base case scenario

This section presents the results of the base case scenario, which assumes normal operation of all the systems and equipment. Figure 1.4 presents how the pressure in the nodes changes during the accident. After the pipe rupture, the pressure in PV starts increasing and in 25 s reaches 1.1 bar, which is a set-point for the 1st burst disk opening. After burst disk opening, the steam is discharged to the piping of venting system and the pressure in PV starts decreasing. Nevertheless, the pressure in PV stays slightly above the atmospheric due to vaporization of the water in PV, which appears due to contact between the water and hot structures. The maximal pressure peak is ~1.11 bar, which means that the diameter of the installed burst disk is sufficient to prevent further pressure increase. Small pressure peak after ~85 s appears due to increased enthalpy of the released coolant (see Figure 1.3), but since the coolant release rate further decreases, the peak is small and short-term.

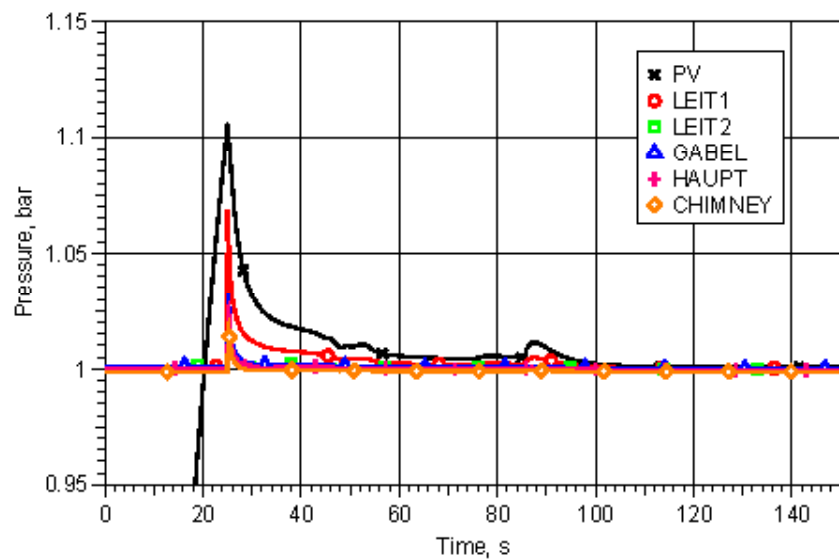


Figure 1.4
Base case scenario:
Pressure in the nodes

Figure 1.5 shows the water mass inside the plasma vessel. After pipe rupture, the water is released to plasma vessel and due to pressure drop partially evaporates. The generated steam contributes to pressure increase in plasma vessel. The water is collected in the lower part of the vessel, but due to contact with hot PV surfaces evaporates as well. The process of vaporization is clearly seen in this figure when after ~70 s the water mass in PV starts decreasing.

Figure 1.6 shows water where most of the steam condenses inside the piping. The largest water mass is observed in node HAUPT, which represents the main pipeline of 500 mm diameter, thus the largest heat transfer area. The other largest part of condensed steam is located in node LEIT1, but no water is observed LEIT2. This result shows that the thickness of the water film on the inner surface of pipes is < 1 mm, and there is no overflow from one node to another.

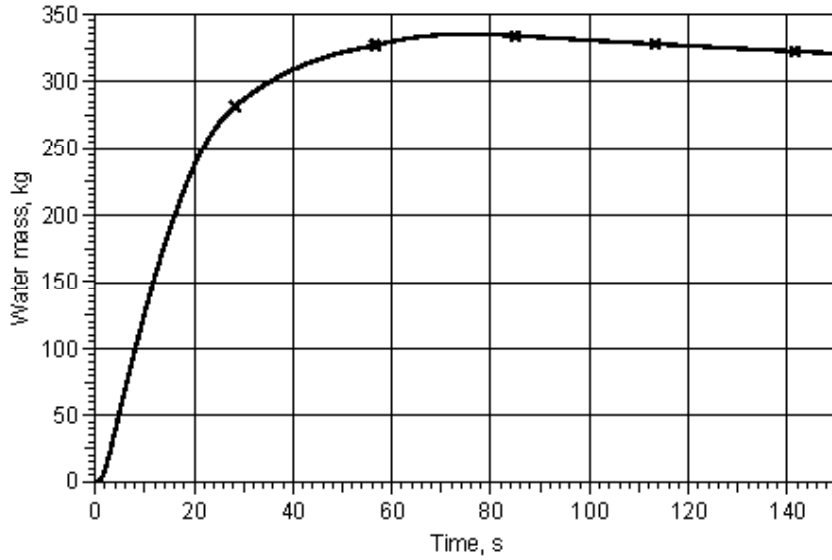


Figure 1.5
Base case scenario:
Water mass in the
plasma vessel

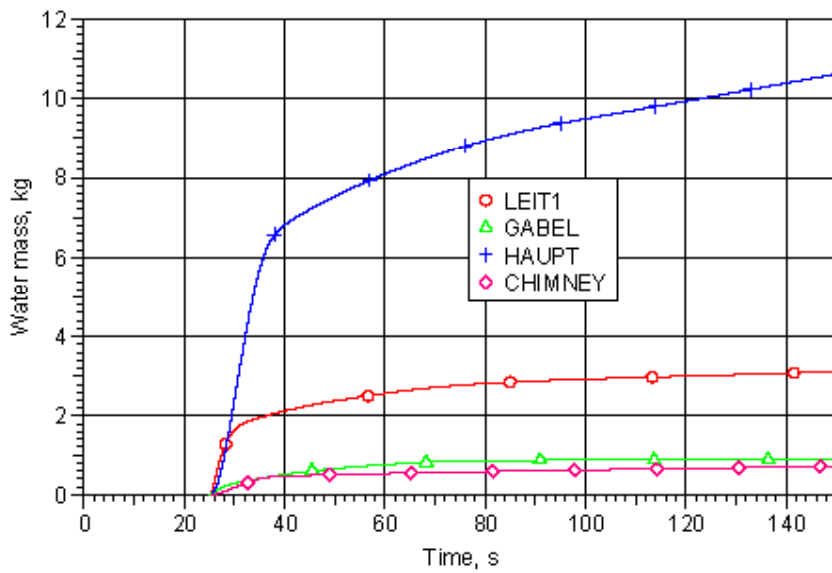


Figure 1.6
Base case scenario:
Water mass in the nodes

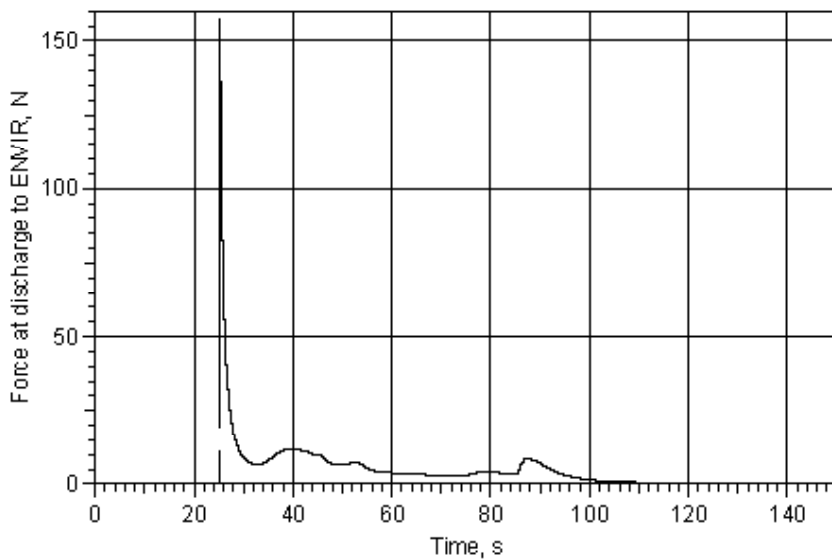


Figure 1.7
Base case scenario: Force
acting at the exit from
venting system to the
environment

To investigate what forces are expected at the exit from the venting system to the environment some additional calculation is required. The force acting on the exit of the exhaust pipe could be expressed by $F = \dot{m}^2 / (\rho \cdot A)$ N, where \dot{m} is the mass flow through the junction (kg/s), ρ is the gas density in CHIMNEY (kg/m³), and A is the area of the junction (d = 500 mm) (m²) The results of the performed calculations using this formula are presented in Figure 1.7. The maximal force is observed right after the burst disk opening and it reaches ~155 N and immediately decreases to a negligible level.

1.3.2 Comparison with RELAP5 results

Analogous calculations are performed using RELAP5 code, which is a thermal-hydraulic code developed for heat and mass transport analysis in the piping systems. This code was used to calculate the coolant release to Plasma Vessel, and further its model was enhanced to simulate the processes in Plasma Vessel and piping of the venting system. RELAP5 solves mass and energy balance equations for each phase (water and gas including steam) separately, i.e. water and steam could have different temperatures, and thermal equilibrium between phases is not required.

One of the main assumptions in the lumped-parameter code COCOSYS is that the water cannot exist in the superheated gas phase. If the water is injected to superheated gas, then its temperature is set equal to saturation temperature at the actual total pressure. The excess energy is used to evaporate water until saturated steam conditions are reached in the gas phase. If the FLUID zone part is not created at that time, then the water remains in the atmosphere as fog, and it is in thermal equilibrium with the gas. If the FLUID part is created, then the water droplets are deposited to this part of the node, i.e. to the sump. Thermal equilibrium between GAS and FLUID parts is not required. In COCOSYS code there are several options to define the coolant injection to the node: 1) injection to the gas phase and 2) injection to FLUID part. In case of injection to FLUID part the injected energy at first is consumed to heat up the sump and then the heat exchange between gas and water occurs via the water surface. The heat exchange with structures associated with GAS and FLUID zone parts is also taken into account.

Figure 1.8 presents comparison between RELAP5 and COCOSYS results using both injection options. Assuming injection to gas phase after pipe rupture the pressure in PV starts increasing

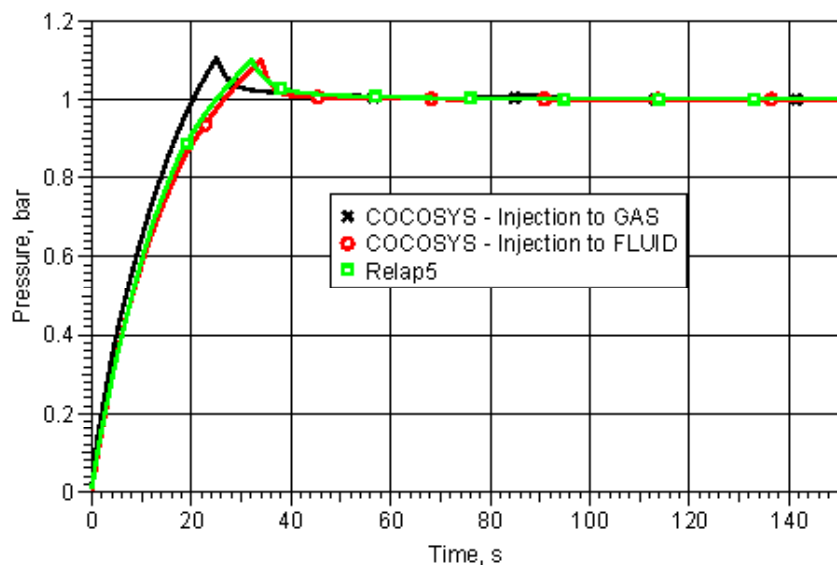


Figure 1.8
Comparison with RELAP5 results: Pressure in the nodes

and in 25 s reaches 1.1 bar, which is a set-point for the 1st burst disk opening. If the injection is assumed to occur to FLUID part, then pressure in PV reaches 1.1 bar in 34 s, and this result is close to RELAP5 results showing 32 s to burst disk opening. The reason for such difference is that the water through the ruptured pipe is assumed to be released to gas phase of PV, which is assumed to be at initial pressure of 1000 Pa, i.e. at such pressure the saturation temperature is close to 0 °C. According to assumption in COCOSYS code, the water temperature is set to saturation temperature at given pressure, and the excess water is evaporated to reach saturated conditions in the gas phase. The water, which is not evaporated, is assumed to be homogeneously distributed in the gas phase. If the water is assumed to be injected to the FLUID part, then the evaporation of water occurs only due to heat exchange between water and gas via the water surface, i.e. much slower process than “flash” evaporation.

Figure 1.9 presents comparison of calculated steam flow through the ruptured burst disk. The largest steam flow is calculated with COCOSYS assuming that injection occurs in the gas phase. The mass flow calculated with RELAP5 code is the smallest (peak is ~2 kg/s) from the three calculated variants, and it shows more oscillations right after rupture of the burst disk.

Figure 1.10 presents comparison of calculated water mass in Plasma Vessel using RELAP5 and COCOSYS codes. RELAP5 results are in agreement with COCOSYS results assuming injection to FLUID part and both of these calculations show more water accumulated in PV compared to the case with water injection to the GAS part of the node. This result clearly shows that the assumption of water injection option influences the received results significantly. The difference between RELAP5 and COCOSYS results assuming injection to GAS is ~50 kg of water in PV.

Figure 1.11 presents comparison of calculated force at discharge point from the venting system to the environment. The largest peak of force occurs in COCOSYS calculations assuming water injection to Plasma Vessel FLUID zone part but it appears after 34 s, the second largest is from COCOSYS calculations assuming water injection to Plasma Vessel GAS zone part. The difference of calculated force at discharge point from the venting system between these variants is ~20 N. The smallest force is calculated with RELAP5 code, which gives only ~50 N at discharge point to environment. These results show that with RELAP5 a much better water deposition and steam condensation along the venting system pipes is calculated compared to COCOSYS.

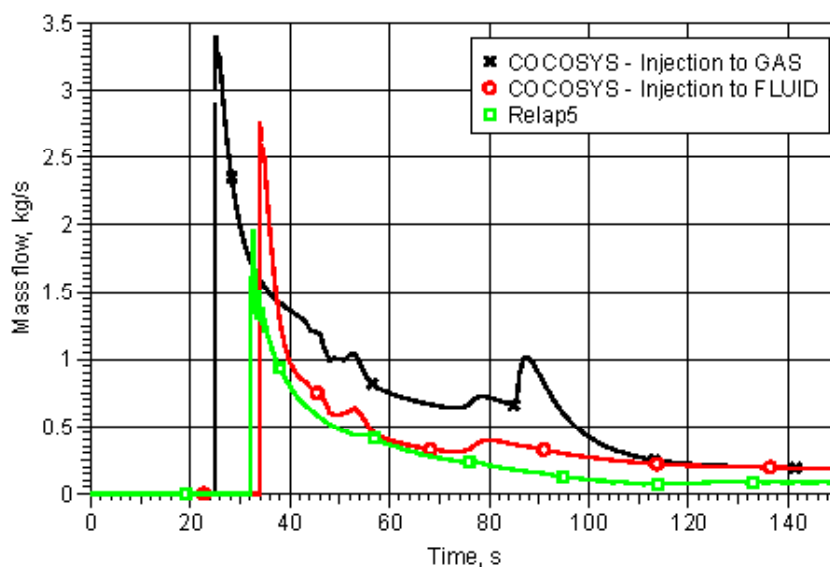


Figure 1.9
Comparison with RELAP5 results: Flow rate through the burst disk

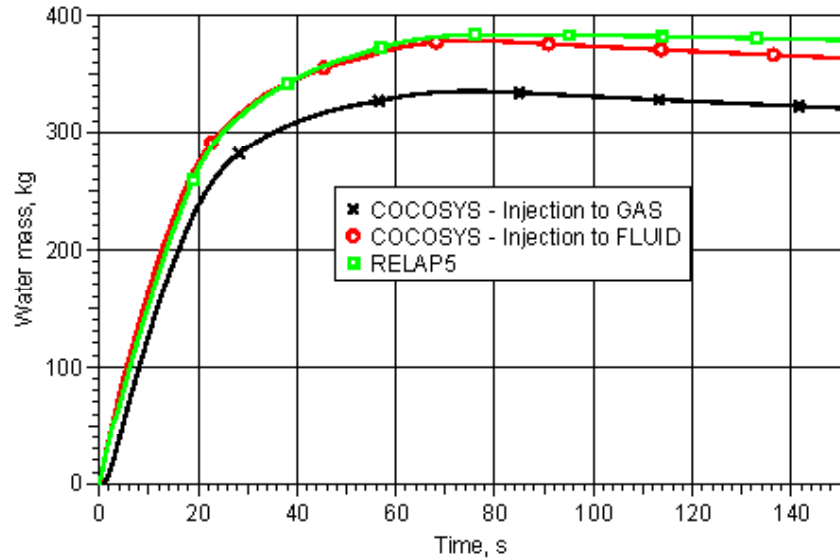


Figure 1.10
Comparison with RELAP5
results: Water mass in PV

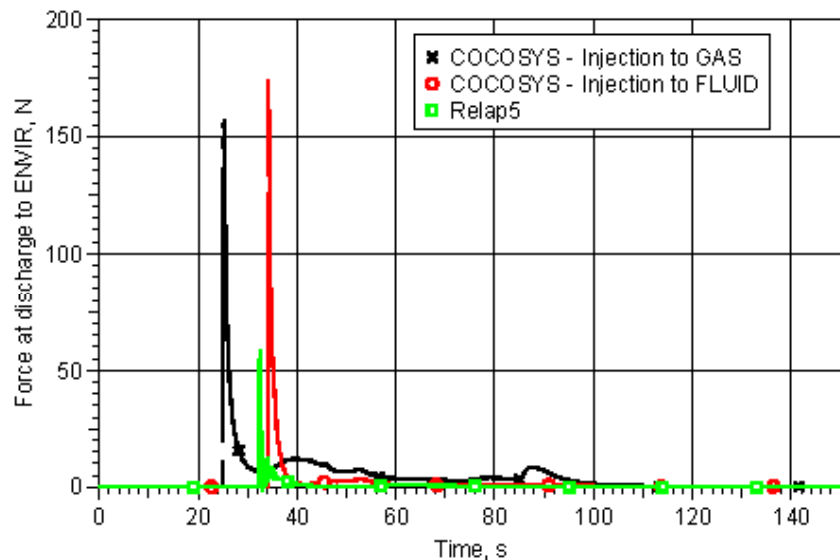


Figure 1.11
Comparison with
RELAP5 results: Force
acting at the exit from
venting system to the
environment

1.4 Failure of opening of burst disk at 1.1 bar

The analysis of a 40 mm pipe rupture inside the Plasma Vessel was performed using COCOSYS code in order to estimate whether the installed burst disks and venting system piping are capable to remove the accident-generated steam from Plasma Vessel during operation in “baking” mode.

The results of the performed analysis showed that:

- If the burst disks open as designed the maximal pressure is 1.11 bar, thus the diameter of the installed burst disk and piping of the venting system ensures prevention of further pressure rise.
- If the first burst disk fails to open, then the maximal pressure in PV is 1.22 bar, thus opening of the second burst disk prevents further pressure rise in pressure vessel.

- The temperature of the outside environment does not have a significant influence on the results.
- The pressure losses in the venting system pipes have only minor influence on maximal pressure in plasma vessel, but they influence depressurization rate, i.e. the larger pressure losses the slower change in pressure is observed.
- The investigated variant with different injection rate given in [1] showed that maximal pressure peak could reach 1.2 bar, but it should be noted that the report does not provide enough details to define the specific enthalpy of the coolant, and it was assumed based on the expected temperature of the released coolant.
- Comparison between COCOSYS and RELAP5 results showed influence of different assumptions in both codes regarding heat and mass exchange processes. RELAP5 Figure 1.21 shows that there is a smaller water mass in the piping when larger

2 LIMIT ANALYSIS OF THE PORT WELDS BETWEEN THE PLASMA VESSEL AND THE PORTS IN THE W7-X CRYOSTAT SYSTEM

The principal investigators for this task are G. Dundulis and R. Karalevičius of LEI.

2.1 Models and boundary conditions

This chapter presents the load scale limit analysis to failure of the welding connections for ports AEU30 and the W7-X Plasma Vessel shell with a 1 mm and 6 mm gap. The geometric model was developed using CAD software SolidWorks. Then the developed geometric model was transferred to Finite Element computer code ABAQUS. These ports were modelled using the FEM technique as 3D bodies together with the regions of the PV shell around the ports and the welding seam. The models were loaded with forces, moments, and pressure provided by IPP and subjected to the load scale limit analysis. The main objective of this analysis was calculation of the limit load scaling factors. The analysis of port weld AEU30 with a 1 mm gap and a 6 mm gap was performed in 2 versions of meshing and 2 versions of calculation step using ABAQUS.

The geometric 3D model of the weld between port AEU30 and the PV shell for a 1 mm gap is presented in Figure 2.1. The finite element models of the welding connection between the port AEU30 and the PV shell were prepared using Finite Element software ABAQUS/Standard and are presented in Figure 2.2. Model of port connection consist of a shell modelled portion PV, a port, and a solid modelled central part (CP). Central part includes a portion of PV and a port and full weld seam (see Figure 2.1b). Analogous models were developed for 6 mm thick weld.

Models of port AEU used linear four node shell elements with reduced integration S4R for shell parts of port and quadratic eight node shell elements with reduced integration S8R of the shell part of PV (see Figure 2.2a). The central part, the part of plasma vessel and the port (see Figure 2.2b) are

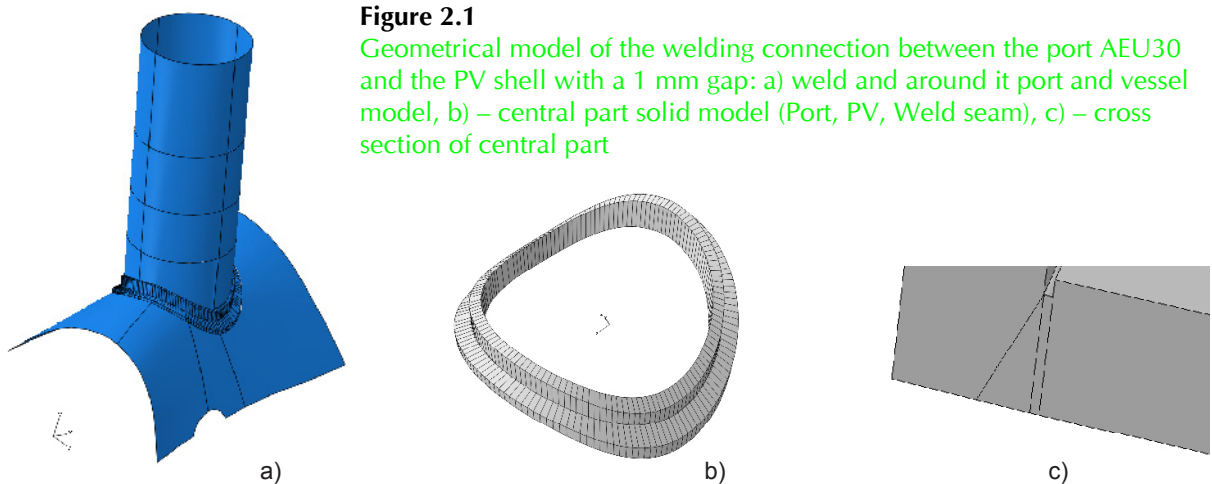


Figure 2.1

Geometrical model of the welding connection between the port AEU30 and the PV shell with a 1 mm gap: a) weld and around it port and vessel model, b) – central part solid model (Port, PV, Weld seam), c) – cross section of central part

Figure 2.2

Finite Element model of the welding connection between the port AEU30 and the PV shell with a 1 mm gap: a) weld and around it port and vessel model, b) – close view of CP meshing

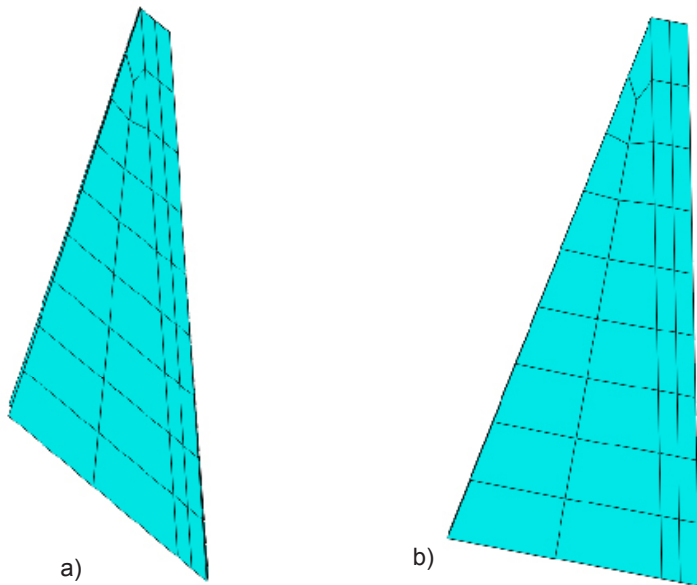
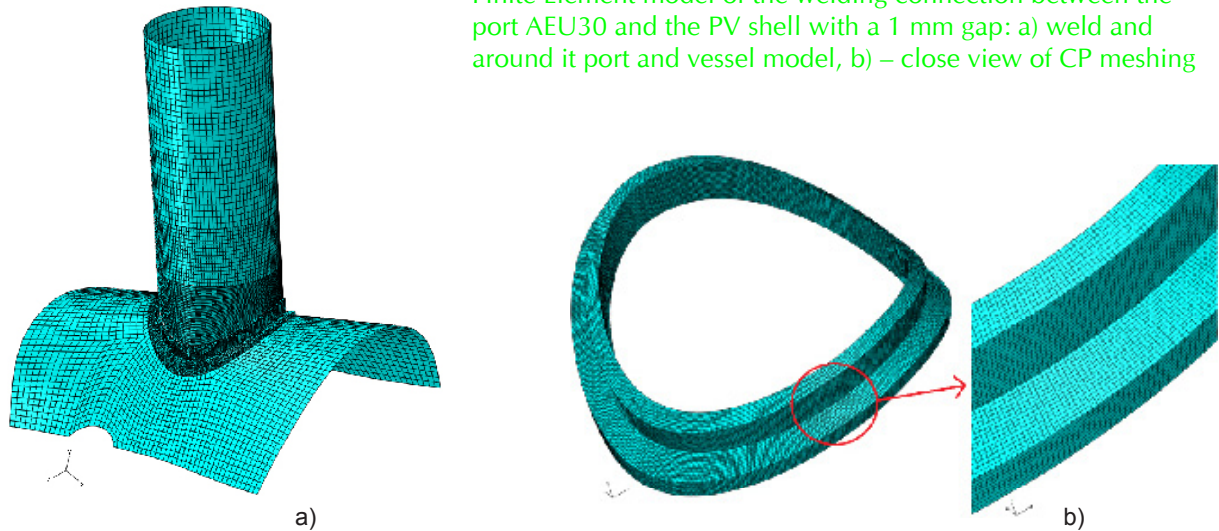


Figure 2.3

Cross sectional view of AEU30 1 mm gap weld seam meshing calculating version v1, v2:
a) $K_{weld} = 0.85$, b) $K_{weld} = 0.7$

modelled as solid, are meshed using a 20-node quadratic brick element with reduced integration C3D20R. Weld seam is meshed using a 20-node quadratic brick element integration C3D20 (see Figure 2.3).

In order to calculate limit load scaling factors, the outer boundaries of the PV (marked red) were constrained in the following way, the displacements of the edges were restricted in all directions, but rotations are allowed. Restrained edges of models shells are highlighted in Figure 2.4.

The loads that were applied at the loading step that corresponds to the loading factor of 1.0 are listed in Table 2.1. "Outer pressure" means that the pressure is applied from the side where the port is attached to the

PV shell. The loads are multiplied with the safety value of 1.2 in order to take possible imprecision of the modelling into account. Safety value of 1.2 is not applied to gravity.

Forces and moments are applied to force-moment addition point called shortly FM. FM point is connected to port end nodes (highlighted magenta) by MPC beam type constrain, shown in Figure 2.5.

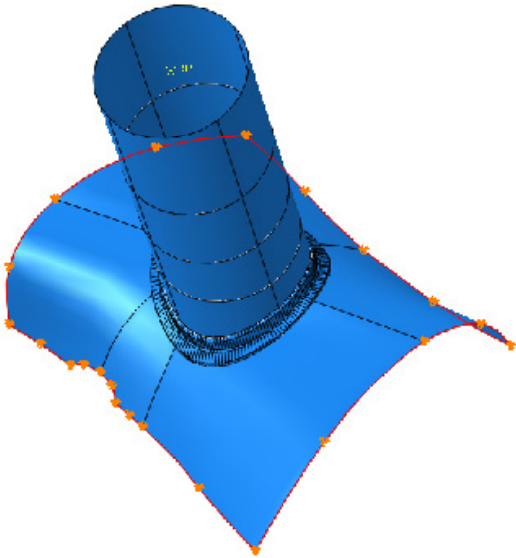


Figure 2.4
Finite Element model boundary conditions of Port AEU

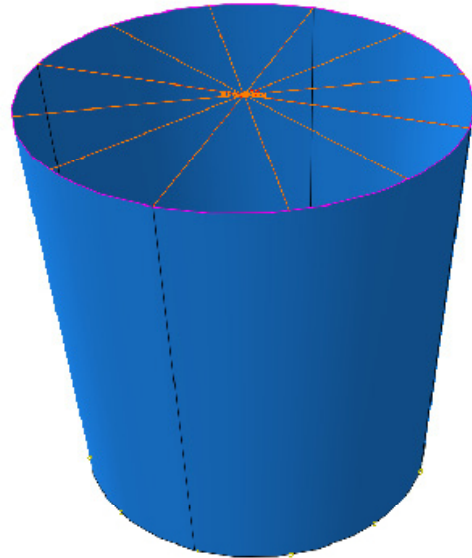


Figure 2.5
FM point coupling to port

The sections of shell parts of port are connected to each other (highlighted red) by tie type constrain shown in Figure 2.6. Shell parts of port and PV are connected to solid center part (highlighted magenta) by shell to solid coupling type constrain, shown in Figure 2.7.

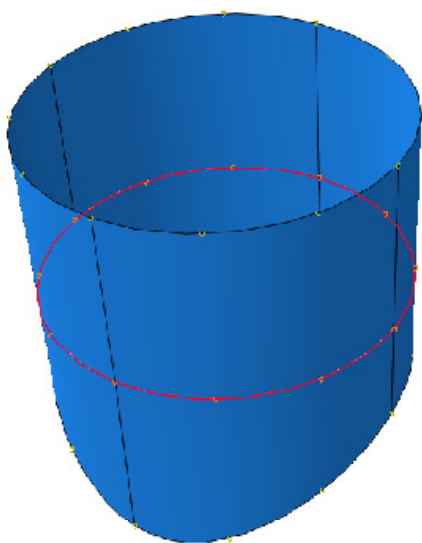


Figure 2.6
Shell-to-Shell coupling

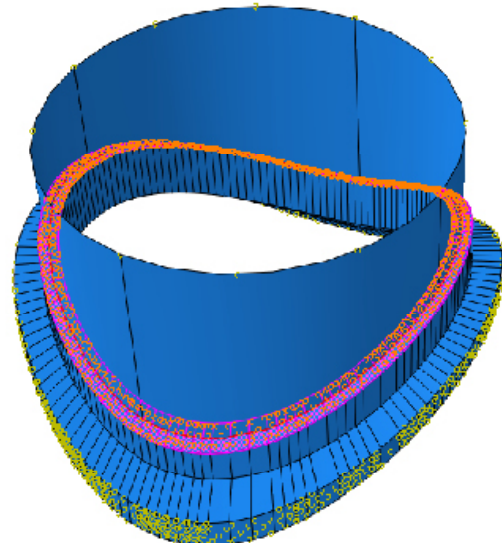


Figure 2.7
Shell-to-Solid coupling

Table 2.1 Loads on the sub-model for the LC 5

<i>Load type</i>	<i>Direction</i>	<i>Port AEU30</i>
Temperature, °C	–	20
Outer pressure, MPa	–	$0.1013 \times 1.2 = \mathbf{0.1216}$
Forces applied the end of the port	$F_{x'}$, kN	$26.034 \times 1.2 = \mathbf{31.241}$
	$F_{y'}$, kN	$-16.458 \times 1.2 = \mathbf{-19.749}$
	$F_{z'}$, kN	$3.515 \times 1.2 = \mathbf{4.218}$
Moments applied the end of the port	$M_{x'}$, kN*mm	$214.009 \times 1.2 = \mathbf{256.811}$
	$M_{y'}$, kN*mm	$4163.394 \times 1.2 = \mathbf{4996.073}$
	$M_{z'}$, kN*mm	$-26504 \times 1.2 = \mathbf{-31804}$

The calculation step increments that were applied at the loading step are listed in Table 2.2. Versions v1 were calculated with biggest possible stable increment, to find out the shape of displacement-SF dependency and specify regions to increased number of points. In case of a 6 mm gap in version v2 the mesh is refined, but calculation strategy is the same. Such approach decreases the calculation time, but in yielding regions there is smaller number of points. Versions v2 in case of a 1 mm gap and v3 in case of a 6 mm gap have divided calculation step increment strategy, in almost linear dependency the biggest increment is used, in yielding region a smaller increment is used, the smallest increment is used in collapse region.

Table 2.2 Step increments of scale factor

<i>Gap, mm</i>	<i>K_{weld}</i>	<i>Version</i>	<i>Mesh size</i>	<i>Scale Factor region</i>	<i>Start incr.</i>	<i>Max incr.</i>
1	0.85	v1	medium	0–9	0.075	0.25
				v2	medium	0–3.5
		3.5–4.2	0.007			0.01
		4.2–4.9	0.003	0.005		
	0.7	v1	medium	0–9	0.075	0.25
				v2	medium	0–3.5
		3.5–3.9	0.007			0.01
		3.9–4.9	0.003	0.005		
6	0.85	v1	coarse	0–9	0.075	0.25
				v2	fine	0–9
		v3	fine			0–3.6
				3.6–4.1	0.007	0.01
		4.1–5.1	0.003	0.005		
		0.85	v1	coarse	0–9	0.075
	v2				fine	0–9
			v3	fine		0–3.3
	3.3–3.7				0.007	0.01
	3.7–4.7		0.003	0.005		

2.2 Results of limit load analysis

The limit load scaling factor analysis of the welding connection between the port AEU30 with a 1 mm gap, 6 mm and the PV shell was performed. The given results are FM point displacement dependency on load Scaling Factor (SF).

The weld material for all ports was chosen as a material with ideal plastification at the level of $1.5 \cdot s_m \cdot K_{\text{weld}}$. Here K_{weld} is a weld efficiency factor. For these welds the values $K_{\text{weld}} = 0.7$ and $K_{\text{weld}} = 0.85$ were taken. The analysis results were presented at both weld efficiency factor values

2.2.1 Results of Port AEU30 with a 1 mm gap

According to limit analysis results in port AEU30 with a 1 mm gap in case the weld efficiency factor values 0.85 load limit SF are 4.4808 for v1 and 4.4828 for v2. In case the weld efficiency factor values 0.7 load limit SF are 4.1493 for v1 and 4.1512 for v2.

Weld efficiency factor $K_{\text{weld}} = 0.85$

In this section, the stress analysis of the welding connection between the port AEU30 and the PV shell using the weld efficiency factor value 0.85 was presented. The history of the displacement of the point where loads are applied during analysis is presented in Figure 2.8.

According to the results of analysis, it was detected that displacement of the point where loads are applied increases linearly until scale factor $SF = 3.5$. The yielding of displacement will occur from $SF = 3.5$ until $SF = 4$. Over $SF = 4$ the displacement starts to increase very rapidly. The convergence of the Finite Element analysis was lost over $SF = 4.4828$ for version of analysis v2 and the stability of port AEU30 with gap 1 mm will be lost. According to this, the limit load will reach at loading factor of 4.4828.

Displacement magnitude distributions at the end step analysis, i.e. $SF = 4.4808$, in this model for version of analysis v1 are presented in Figure 2.9. Maximal displacement magnitude 28.23 mm is obtained on the wall of the port.

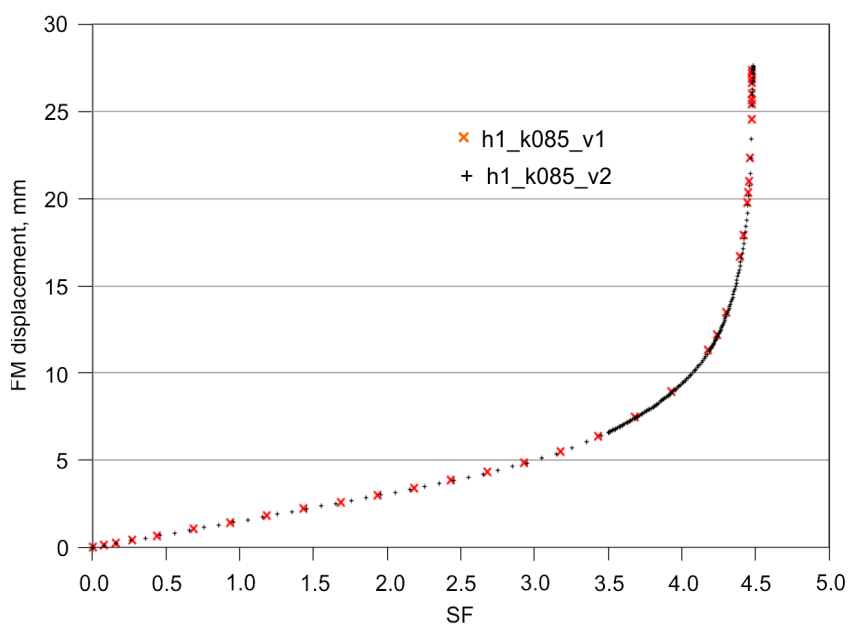


Figure 2.8
Displacement
of force-
moment
addition point

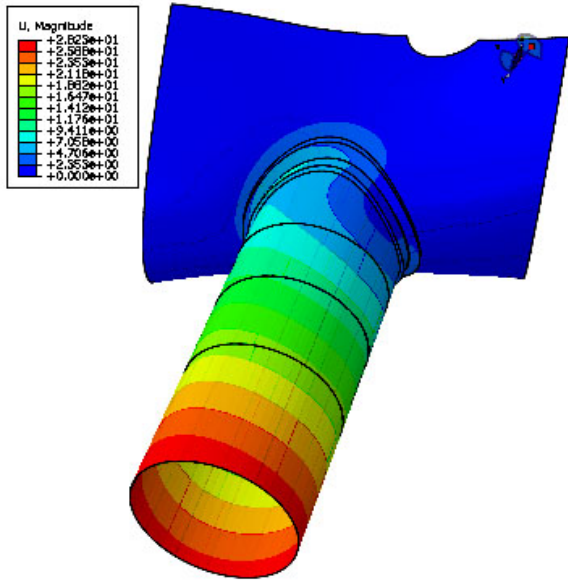


Figure 2.9
Distribution of displacement in model
AEU30 h1 k085 v1

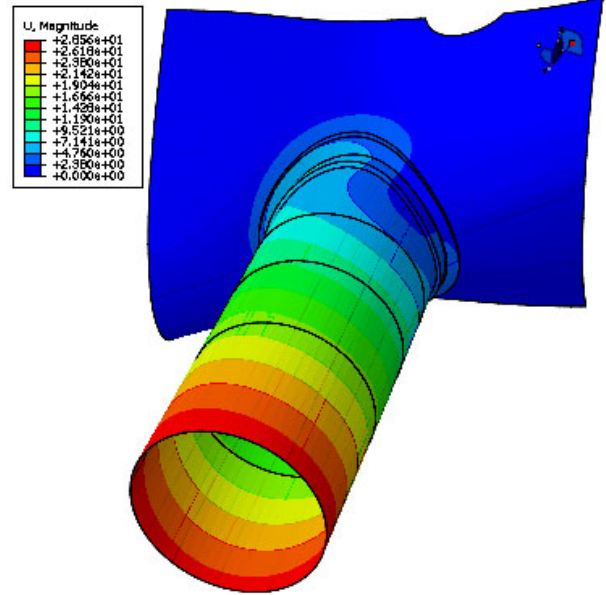


Figure 2.10
Distribution of displacement in model
AEU30 h1 k085 v2

Displacement magnitude distributions at the end step analysis, i.e. SF = 4.4828, in this model for version of analysis v2 are presented in Figure 2.10. Maximal displacement magnitude 28.56 mm is obtained on the wall of the port.

Stress distributions in model in the welding between Plasma Vessel and ports AEU30 with a 1 mm gap at the end step analysis, i.e. SF = 4.4828, for version of analysis v2 are presented in Figure 2.11. It was received that the stresses in port AEU30 and vessel exceed the yield strength, which is 320 MPa, and the stresses in weld also exceed the yield strength which is 272 MPa.

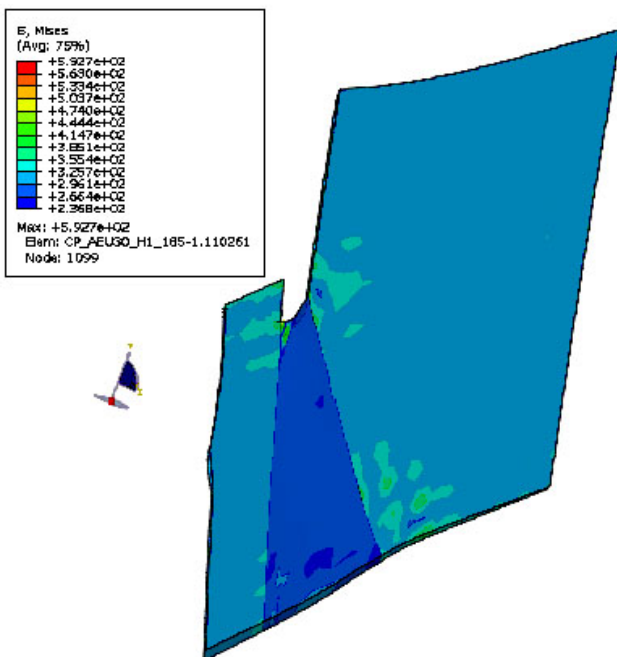


Figure 2.11
Distribution of von Mises stress in model
AEU30 h1 k085 v2 central part cross section
trough weld maximal stress value

The distribution of equivalent plastic strain at the port and PV around weld, and weld are presented in Figure 2.12. The equivalent plastic strain zones are located in the weld seams. It is seen that special attention should be paid for the inspection of the weld tip as it is a place of stress and strain concentrations.

According to the stress and equivalent plastic strain results, it is possible to maintain that failure of the port will have a ductile character.

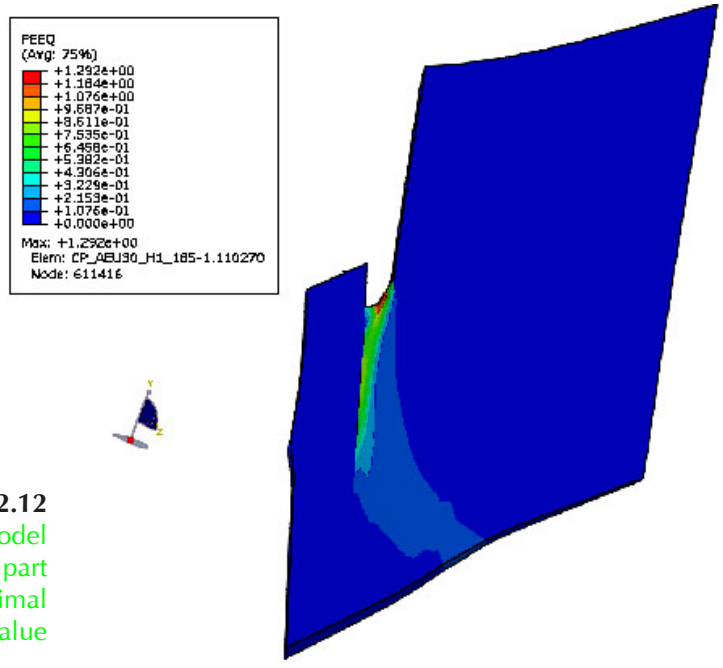


Figure 2.12
Distribution of PEEQ in model AEU30 h1 k085 v2 central part cross section trough weld maximal stress value

Weld efficiency factor $K_{weld} = 0.7$

In this section, the stress analysis of the welding connection between the port AEU30 and the PV shell using the weld efficiency factor value 0.7 was presented. The history of the displacement of the point where loads are applied during the analysis is presented in Figure 2.13.

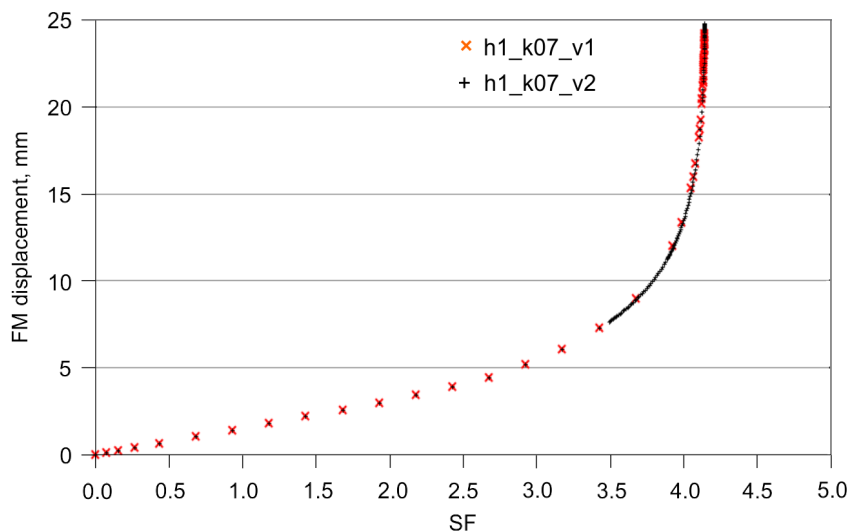


Figure 2.13
Displacement of force-moment addition point

According to the results of the analysis, it was detected that displacement of the point where loads are applied increases linearly until scale factor $SF = 3.2$. The yielding of displacement will occur from $SF = 3.2$ until $SF = 3.7$. Over $SF = 3.7$ the displacement starts to increase very rapidly. The convergence of the Finite Element analysis was lost over $SF = 4.1512$ for version of analysis v2 and the stability of port AEU30 with a 1 mm gap will be lost. According to this, the limit load will be reached at loading factor of 4.1512.

Displacement magnitude distributions at the end step analysis, i.e. $SF = 4.1493$, in this model for version of analysis v1 are presented in Figure 2.14. Maximal displacement magnitude 24.98 mm is obtained on the wall of the port.

Displacement magnitude distributions at the end step analysis, i.e. $SF = 4.1512$, in this model for version of analysis v2 are presented in Figure 2.15. Maximal displacement magnitude 25.62 mm is obtained on the wall of the port.

Stress distributions in model in the welding between Plasma Vessel and ports AEU30 with a 1 mm gap at the end step analysis, i.e. $SF = 4.1512$, for version of analysis v2 are presented in Figure 2.16. It was received that the stresses in port AEU30 and vessel exceed the yield strength, which is 320 MPa, and the stresses in weld also exceed the yield strength, which is 224 MPa.

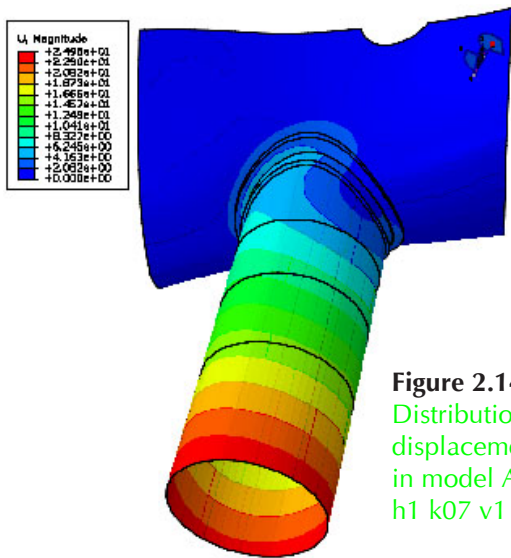


Figure 2.14
Distribution of displacement in model AEU30 h1 k07 v1

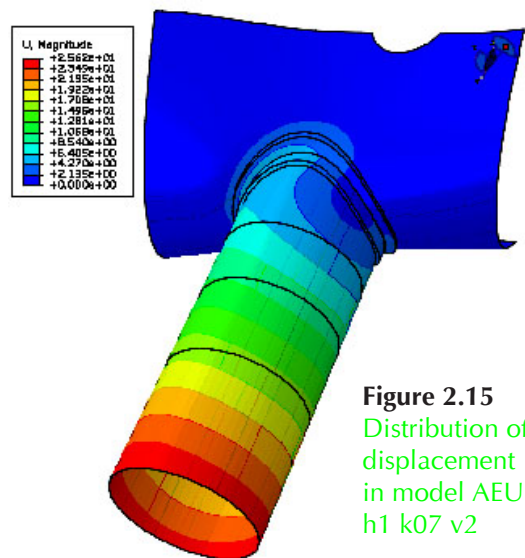


Figure 2.15
Distribution of displacement in model AEU30 h1 k07 v2

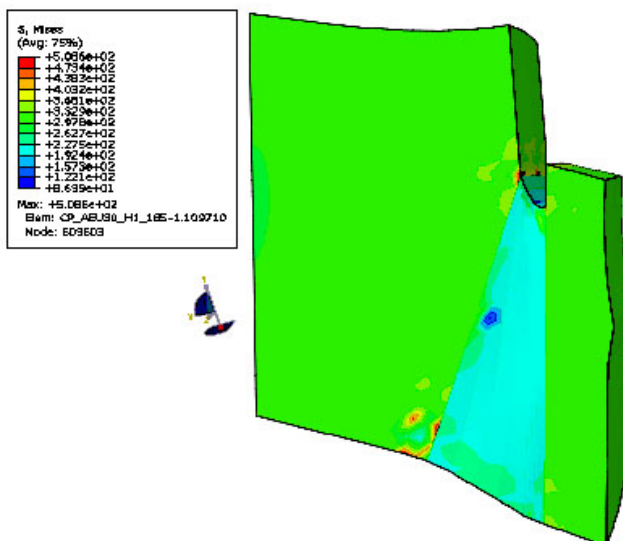


Figure 2.16
Distribution of von Mises stress in model AEU30 h1 k07 v2 central part cross section trough weld maximal stress value

The distribution of equivalent plastic strain at the port and PV around weld, and weld are presented in Figure 2.17. The equivalent plastic strain zones are located in the weld seams. It is seen that special attention should be paid for the inspection of the weld tip as it is a place of stress and strain concentrations.

According to the stress and equivalent plastic strain results, it is possible to maintain that failure of the port will have a ductile character.

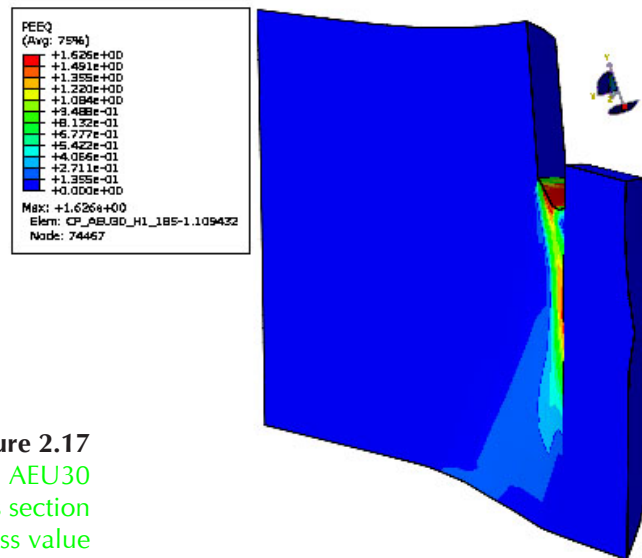


Figure 2.17
Distribution of PEEQ in model AEU30
h1 k07 v2 central part cross section
trough weld maximal stress value

2.2.2 Results of Port AEU30 6 mm gap

According to limit analysis results in port AEU30 with a 6 mm gap in case the weld efficiency factor values 0.85 load limit SF are 4.3603 for v1, 4.3420 for v2, 4.3454 for v3. In case the weld efficiency factor values 0.7 load limit SF are 3.9926 for v1, 3.9747 for v2, 3.9756 for v3.

Weld efficiency factor $K_{weld} = 0.85$

In this section, the stress analysis of the welding connection between the port AEU30 and the PV shell using the weld efficiency factor value 0.85 was presented. The history of the displacement of the point where loads are applied during the analysis is presented in Figure 2.18.

According to the results of the analysis, it was detected that displacement of the point where loads are applied increases linearly until scale factor SF = 3.4. The yielding of displacement will occur from SF = 3.4 until SF = 3.9. Over SF = 3.9 the displacement starts to increase very rapidly. The convergence of the Finite Element analysis was lost over SF = 4.3454 for version of analysis v3, and the stability of port AEU30 with a 6 mm gap will be lost. According to this, the limit load will be reached at loading factor of 4.3454.

Displacement magnitude distributions at the end step analysis, i.e. SF = 4.3603, in this model for version of analysis v1 are presented in Figure 2.19. Maximal displacement magnitude 30.27 mm is obtained on the wall of the port.

Displacement magnitude distributions at the end step analysis, i.e. SF = 4.3420, in this model for version of analysis v2 are presented in Figure 2.20. Maximal displacement magnitude 30.01 mm is obtained on the wall of the port.

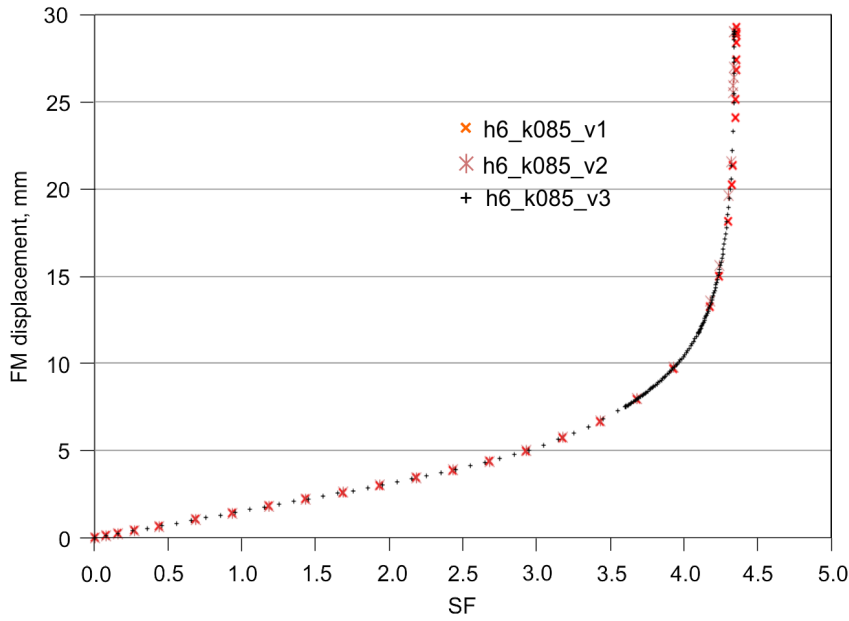


Figure 2.18
Displacement of force-moment addition point

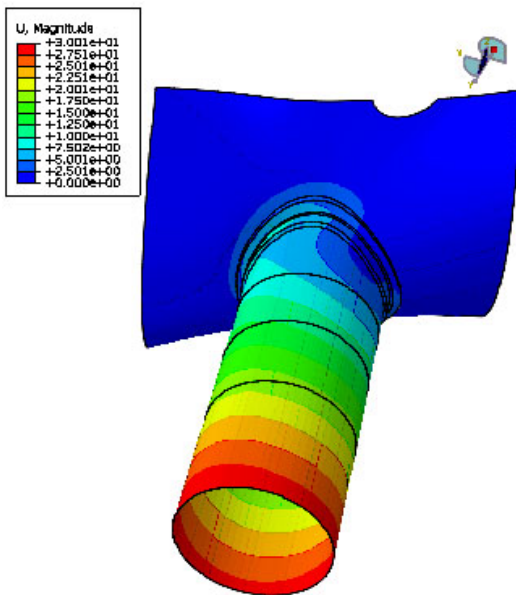


Figure 2.19
Distribution of displacement in model AEU30 h6 k085 v1

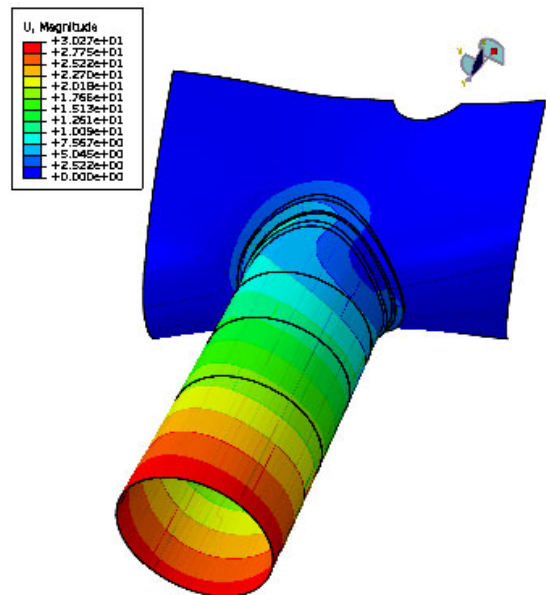


Figure 2.20
Distribution of displacement in model AEU30 h6 k085 v2

Displacement magnitude distributions at the end step analysis, i.e. SF = 4.3454, in this model for version of analysis v3 are presented in Figure 2.21. Maximal displacement magnitude 30.03 mm is obtained on the wall of the port.

Stress distributions in model in the welding between Plasma Vessel and ports AEU30 with a 6 mm gap at the end step analysis, i.e. SF = 4.3454, for version of analysis v3 are presented in Figure 2.22. It was received that the stresses in port AEU30 and vessel exceed the yield strength, which is 320 MPa, and the stresses in weld also exceeds the yield strength, which is 272 MPa.

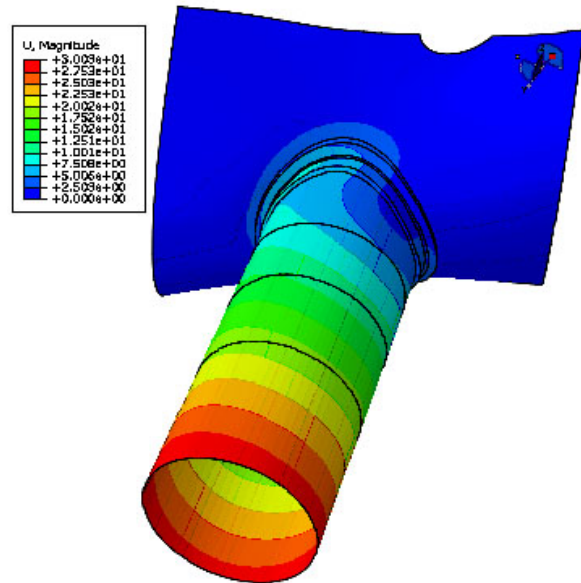


Figure 2.21
Distribution of displacement in model AEU30 h6 k085 v3

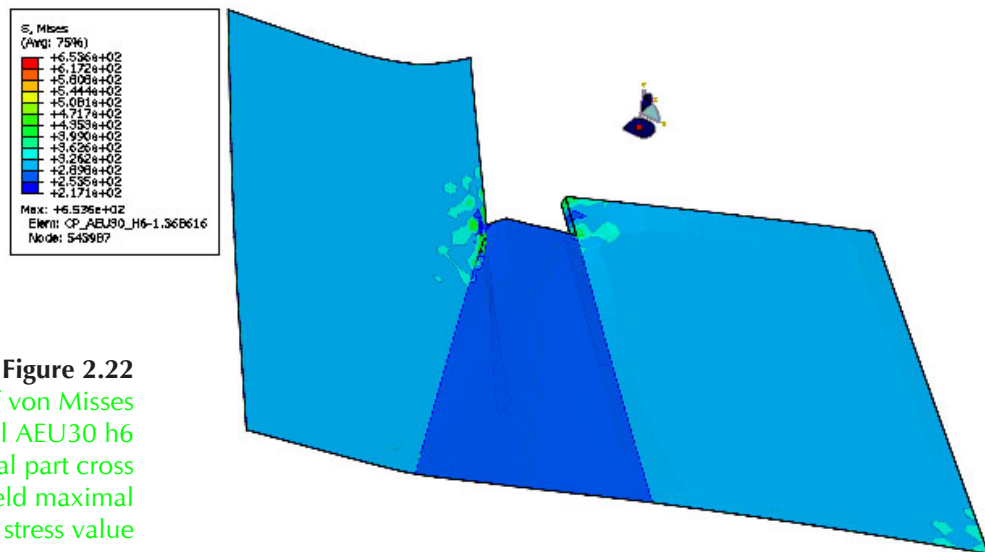


Figure 2.22
Distribution of von Mises stress in model AEU30 h6 k085 v3 central part cross section trough weld maximal stress value

The distribution of equivalent plastic strain at the port and PV around weld, and weld are presented in Figure 2.23. The equivalent plastic strain zones are located in the weld seams. It is seen that special attention should be paid for the inspection of the weld tip as it is a place of stress and strain concentrations.

According to the stress and equivalent plastic strain results, it is possible to maintain that failure of the port will have a ductile character.

Weld efficiency factor $K_{weld} = 0.7$

In this section, the stress analysis of the welding connection between the port AEU30 and the PV shell using the weld efficiency factor value 0.7 was presented. The history of the displacement of the point where loads are applied during analysis is presented in Figure 2.24.

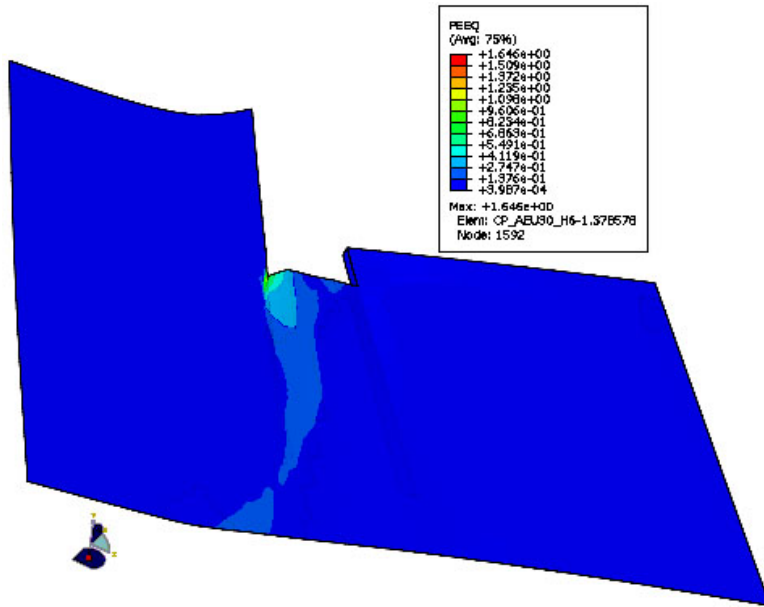


Figure 2.23
Distribution of PEEQ in model AEU30 h6 k085 v3 central part cross section trough weld maximal stress value

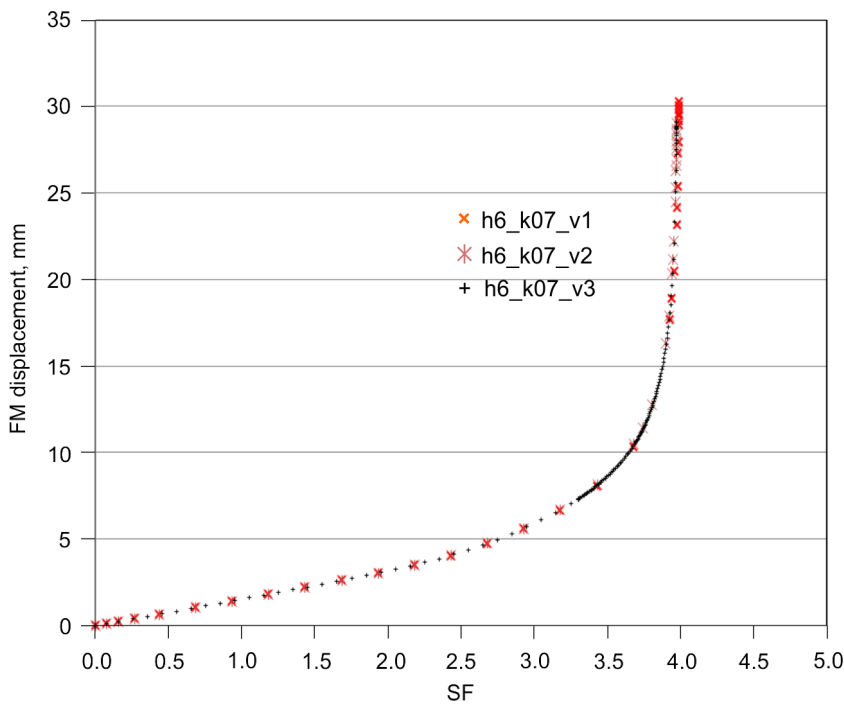


Figure 2.24
Displacement of force-moment addition point

According to the results of analysis, it was detected that displacement of the point where loads are applied increases linearly until scale factor $SF = 2.9$. The yielding of displacement will occur from $SF = 2.9$ until $SF = 3.5$. Over $SF = 3.5$ the displacement starts to increase very rapidly. The convergence of the Finite Element analysis was lost over $SF = 3.9756$ for version of analysis v3, and the stability of port AEU30 with a 6 mm gap will be lost. According to this, the limit load will be reached at loading factor of 3.9756.

Displacement magnitude distributions at the end step analysis, i.e. $SF = 3.9926$, in this model for version of analysis v1 are presented in Figure 2.25. Maximal displacement magnitude 31.32 mm is obtained on the wall of the port.

Displacement magnitude distributions at the end step analysis, i.e. SF = 3.9747, in this model for version of analysis v2 are presented in Figure 2.26. Maximal displacement magnitude 30.00 mm is obtained on the wall of the port.

Displacement magnitude distributions at the end step analysis, i.e. SF = 3.9756, in this model for version of analysis v3 are presented in Figure 2.27. Maximal displacement magnitude 30.07 mm is obtained on the wall of the port.

Stress distributions in model in the welding between Plasma Vessel and ports AEU30 with a 6 mm gap at the end step analysis, i.e. SF = 3.9756, for version of analysis v3 are presented in Figure 2.28. It was received that the stresses in port AEU30 and vessel exceed the yield strength, which is 320 MPa, and the stresses in weld also exceed the yield strength, which is 224 MPa.

The distribution of equivalent plastic strain at the port and PV around weld, and weld are presented in Figure 2.29. The equivalent plastic strain zones are located in the weld seams. It is seen that special attention should be paid for the inspection of the weld tip as it is a place of stress and strain concentrations.

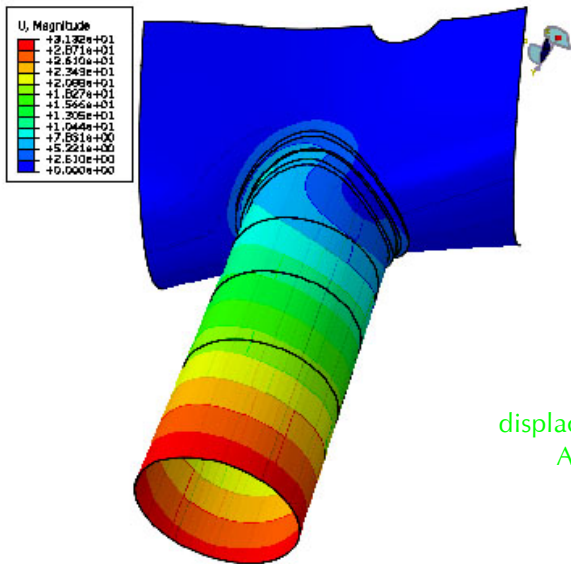


Figure 2.25
Distribution of displacement in model AEU30 h6 k07 v1

Figure 2.26
Distribution of displacement in model AEU30 h6 k07 v2

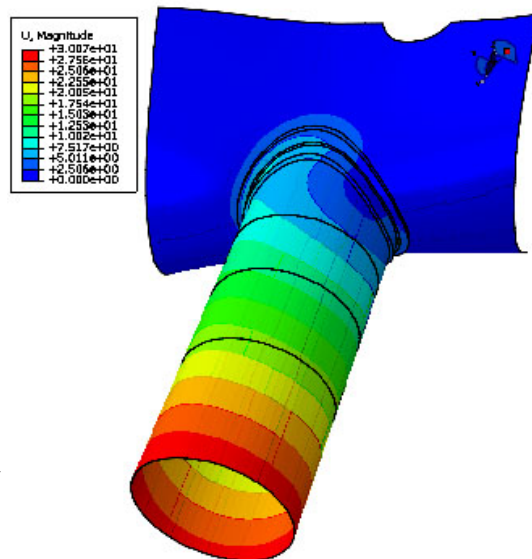
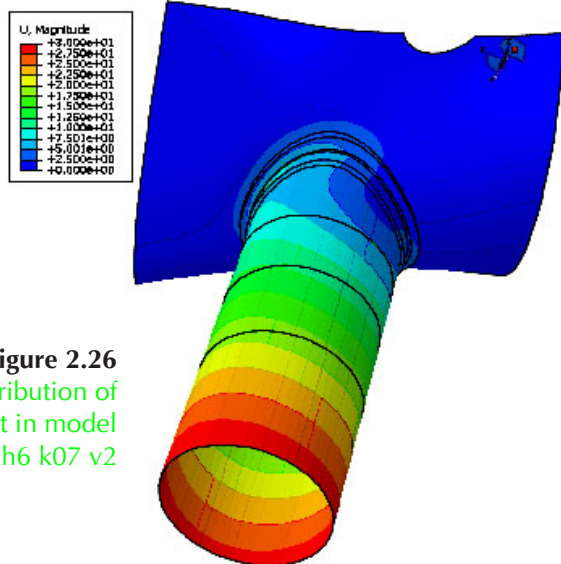


Figure 2.27
Distribution of displacement in model AEU30 h6 k07 v3

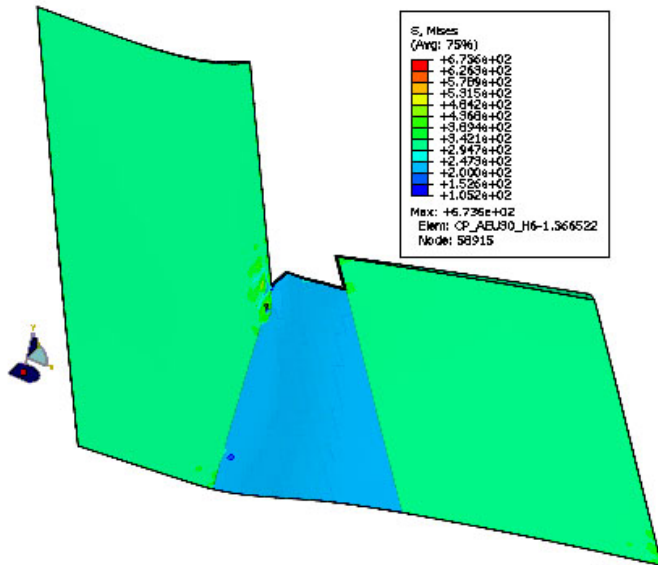


Figure 2.28
Distribution of von Mises stress in model AEU30 h6 k07 v3 central part cross section trough weld seam maximal stress value

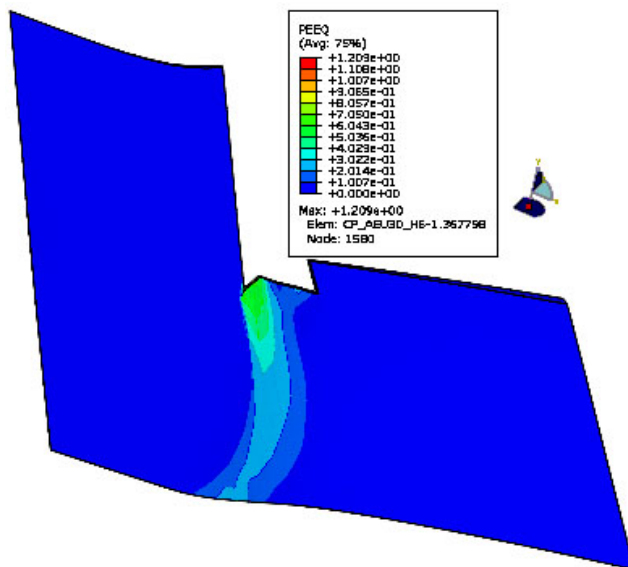


Figure 2.29
Distribution of PEEQ in model AEU30 h6 k07 v3 central part cross section trough maximal stress value

According to the stress and equivalent plastic strain results, it is possible to maintain that failure of the port will have a ductile character.

2.3 Summary of limit load analysis

The analysis of the welding connection between the port AEU30 and the PV with 1 mm and 6 mm gaps, for limit load scale factor was performed. For these welds the weld efficiency factor values $K_{weld} = 0.7$ and $K_{weld} = 0.85$ were used.

From the displacement dependency presented in Figure 2.8, Figure 2.13, Figure 2.18, and Figure 2.24, it is seen that increasing the gap between port and PV, or decreasing weld efficiency decreases the limit load Scaling Factor. The convergence was lost in the end of analysis; the last calculated point is load limit SF.

According to limit analysis results in port AEU30 with a 1 mm gap in case the weld efficiency factor values 0.85 and 0.7 limit scale factor 4.48 and 4.15. Results in port AEU30 with a 6 mm gap in case the weld efficiency factor values 0.85 and 0.7 limit scale factor 4.34 and 3.97. According to the results of the analysis, it is possible to conclude that the stability of the welding between Plasma Vessel and ports AEU30 with a 1 mm and 6 mm gap will be sustained to the end value of load SF.

3 W7-X PROBABILISTIC RISK ANALYSIS

The principal investigators for this task are R. Alzbutas and R. Voronov of LEI.

During the plasma experiments, the magnetic coils of the stellarator are cooled to extremely low temperatures (4 K) in order to ensure superconductivity. When the plasma operation stops, residual cold may freeze the water circuits if the water circulation is stopped. There are a number of possible reasons for the loss of circulation, the loss of power supply of circulating pumps among them. Emergency power supply system of W7-X is equipped with diesel generator, which automatically starts within 15 s after loss of external grid. If the emergency power supply fails, there is no possibility to ensure water circulation and to avoid freezing; the water from the cooling circuits should be drained.

Freezing of water circulation circuits may lead to the rupture of cooling lines. Although the plasma vessel itself and the ports are expected not to be affected, further operation is not possible and the searching of the leak due to the restricted accessibility may lead to inability of W7-X device for experiments for a long period of time.

There are different possible reasons for the loss of water circulation in the cooling circuits, e.g. failure of pumps, blockage of water lines, loss of power supply to the pumps, fire, etc. Loss of external power supply was chosen in order to provide an example of accident sequence analysis, which may be applied to W7-X safety analysis.

There are a number of water-cooling circuits, which ensure cooling of plasma vessel components:

- Target cooling circuit ACK10.
- Baffle/Wall cooling circuit ACK20.
- Plasma vessel/ ports cooling circuit ABK10.
- Regulation coils cooling circuit ACK30/AAR10.
- ECB50.

In case of loss of water circulation, the plasma vessel/ports cooling circuit ABK10, which is located close to the cold cryostat, may freeze.

According to estimations performed by IPP, the time of freezing is:

- ~3 days (66 hours), if the heat capacity of the plasma vessel is considered, i.e. equal temperature of plasma vessel and connected pipes due to the good thermal contact.
- within 5 hours, if single (not thermally connected) pipes filled with water are considered
- within 10-15 min, if together with the circulation loss (double failure) also a significant pressure increase in the cryostat occurs, e.g. due to a large He leak.
- RT chevrons of the cryopumps, which are also supplied by ABK10, freeze in about 50 min.

To prevent the freezing, if both pumps ABK10-AP001 and ABK10-AP002 fail, then the pump of the trim coils cooling circuit AAR10 will be automatically connected to ABK10 and will ensure water circulation.

The power supply is provided from 110/20 kV and 20 kV grids that are quite independent; however, both grids are supplied from one external remote station. It is known that the failure in this station in 2010 caused power outage of both grids. In case of loss of power from external (general) network,

an automatic signal to start Emergency Diesel Generator (EDG) is generated. A manual startup of the EDG is also possible. EDG reaches a full capacity in 15 seconds after the start.

Cooling circuit pumps ABK10-AP001 and ABK10-AP002 stop after the loss of power. When the power supply from the EDG is restored, the pumps are restarted automatically. Manual start of the pumps is also available.

For the analysis, it was assumed that the accident starts with the loss of offsite power (LOSP) supply from 110/20 kV network. The reason for the LOSP could be system failure, network instability, extreme weather, etc. This is an initiating event (IE) of the accident sequence. The IE "LOSP" is indicated on the left side of the ET (see Figure 3.1).

Scenario 1 (successful)

On the loss of power supply, an automatic signal to start up the EDG is generated and the EDG reaches its full capacity within 15 seconds. If automatic startup fails, the manual start of the EDG is possible. This is modelled by branching point for the FE "EDG startup".

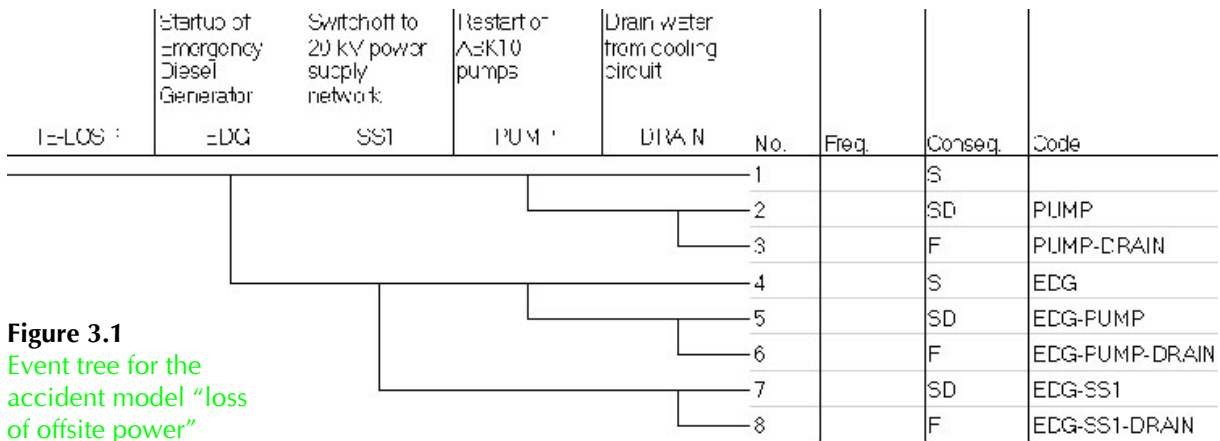


Figure 3.1
Event tree for the accident model "loss of offsite power"

After a successful start of EDG and power restoration at SN (right branch of the ET), the pumps of the water-cooling circuits should be restarted automatically or (as a backup) manually.

After a successful start of pumps, the water circulation should be provided to avoid freezing. This is modelled by branching point for the FE "Pumps startup".

Required operation time of the pumps is assumed 24 hours until the power supply network is restored.

When start and operation of the pumps is successful (right branch of the ET), the accident scenario ends in a safe state and the consequence is "Safe". This is sequence number 1 (Sq 1) of the event tree.

Scenario 2 (failure of EDG and switch to alternative power source)

If both automatic and manual startup of EDG fail (down branch for the FE "EDG startup"), there is still a possibility to provide power supply from busbar SS1. Of course this is possible only in the case when power supply of SS1 from 20 kV network is not affected by the Initiating event. This is modelled by branching point for the FE "switch to SS1".

After this, the sequence continues as sequence 1 and ends with the "safe" state. See sequence 4.

Scenario 3 (failure to restart circulation)

If attempts to restart power supply or cooling circuits fail (this is modelled by down branch for the FE “Pumps startup”), there is a risk of coolant freezing due to accumulated cold of the extremely cooled parts of the stellarator. The only way to prevent such freezing and avoid the ruptures is to drain the water from the cooling circuits. This operation is performed manually. This is modelled by branching point for the FE “Drain circuits”.

When the water is successfully drained (right branch of the ET), the freezing is avoided, but then more time is required to fill the circuits again in order to continue W7-X operation. The accident scenario ends in a safe state, but the consequence is therefore “Safe drained”.

Scenario 4 (failure to drain water)

If an attempt to empty the cooling circuits fails (this is modelled by down branch for the FE “Drain circuits”), then nothing could prevent the coolant freezing and subsequent ruptures. The accident scenario ends with a failure of the frozen components and the consequence is therefore “Failure”. See sequences 3, 6, 8. The initiating event is modelled with a single basic event “Loss of offsite power” with frequency 3.5×10^{-5} 1/hour, i.e. 0.31 1/year.

The calculation was made for the consequence “Failure” of the event tree. The “optimistic” values of human error probabilities, which do not account for actual personnel availability, were used. As a result of the event tree analysis Minimal Cut Sets (MCS) are generated.

The calculated failure frequency to avoid ABK10 freezing in case of loss of power supply is 2.56×10^{-3} 1/year. Dividing this number by the initiating event frequency the “safety barrier” could be calculated:

$$SB = F(C)/F(IE) = 2.56 \times 10^{-3} / 3.07 \times 10^{-1} = 8.34 \times 10^{-3}.$$

This figure means the conditional probability of the consequence in case of initiating event. In the considered case it means how many circuit freezings may be expected during losses of power supply. The result shows only about 8 freezing in case of 1000 LOSP. However, it would not be correct to interpret this figure in the way that the freezing may happen in 120 LOSP, which would be more than the entire lifetime of the W7-X. One should remember that this is an average indicative value, and the freezing may happen in the very first case of LOSP or not happen at all.

As a result of the event, tree model analysis 21 minimal cut sets were generated. Explanation of six top accident scenarios leading to the failure is presented in Table 3.1. The remaining MCS bring less than 11% to the total accident frequency.

The results show a rather high safety barrier against the initiating event. It should be said that such result would be absolutely unacceptable for a nuclear power plant where a frequency of reactor core damage is calculated. For this case, however, the consequences are incomparably lower.

If it is decided to improve the W7-X protection against such specific accident, the provided importance indicators show the priorities for such improvements. Among the front line systems, the reliability of Emergency Diesel Generator should be improved. Reliability of the grid itself is also important; however, such improvement could be a subject of discussion with the power supply company.

Emptying of ABK10 circuit starting with water chevron circuits as the “last chance” measure is impossible due to long time required. Making this operation less time-consuming would increase the system protection against freezing.

Table 3.1. Top accident scenarios

<i>No</i>	<i>Probability</i>	<i>%</i>	<i>Scenario description</i>
1	7.99×10^{-4}	31.20	EDG fails to run; Human error to switch to SS1; human error to empty ABK10
2	5.94×10^{-4}	23.20	Both ABK10 pumps fail to start; human error to empty ABK10
3	5.32×10^{-4}	20.80	Failure of both networks; EDG fails to run; human error to empty ABK10
4	1.61×10^{-4}	06.30	Automatic switch of ABK10 pumps to Secure Network fail; Human Error to manually switch ABK10 pumps to SN; Human error to empty ABK10
5	1.20×10^{-4}	04.68	EDG fails to start; Human error to switch to SS1; Human error to empty ABK10
6	7.97×10^{-5}	03.12	Failure of both networks; EDG fails to start; Human error to empty ABK10

The human reliability analysis performed in scope of this work emphasizes the measures that could be taken to improve the operators' ability to cope with accidents. First measure is to provide written emergency procedures. The next would be to consider availability of the necessary personnel 24/7. This might be done either by increasing the number of shifts or, as less consuming way, to train CCR operators to perform most safety important actions by themselves when the TS is unavailable. The technical measures, which make operators' performance easier, e.g. good indication of failures, good communication and even the light torches would also increase personnel reliability.

On the other hand, it might be a case that too expensive safety improvement measures may outweigh the prevented losses from the accident. The feasibility analysis and prioritization of safety measures from the costs point of view could be recommended.

The following recommendations are provided to increase the protection against freezing in case of loss of off-site power:

- Consider 24/7 personnel availability.
- Develop emergency procedures and keep emergency training.
- Provide clear indications and alarms for the critical equipment.
- Provide personnel with torches or consider emergency lighting from batteries. Provide communication equipment independent on power supply.
- Indicate in the emergency procedures that in case of loss of circulation the cryopumps must be drained first. Provide easy access to the valves in order to minimize draining time.

4 THEORETICAL INVESTIGATION FOR PLASMA DIAGNOSTICS

Principal investigators in this task are P. Bogdanovich, G. Gaigalas and R. Karazija of VU ITPA.

During **2011** investigations were performed as follows:

- The applicability of quasirelativistic approach has been investigated by performing the theoretical studies of the spectroscopic parameters of multicharged tungsten ions having open 4d-shell. Calculations were performed in quasirelativistic approximation with extensive inclusion of correlation effects. It was demonstrated that this approach enables achieving accuracy not worse than the accuracy of the completely relativistic *ab initio* calculation results.
- The calculation of fluorescence yields, Auger transition probabilities and natural level widths for the states of multiple ions of tungsten with vacancies in the 4ℓ ($\ell = 0-3$) were carried out. The Auger transitions in the low and middle charged tungsten ions from the initial states with vacancies in the 4s, $4p_{1/2}$, $4p_{3/2}$, $4d_{3/2}$, $4d_{5/2}$ subshells and 4f shell were considered. The calculations of radiative transition spectra in the regions of 4–7 nm and 12–14 nm for $W^{40+} - W^{45+}$ and electron-impact excitation rates among the levels of 4dN configurations for tungsten ions were also performed.
- Large-scale nonrelativistic and relativistic calculations of the lowest 997 energy levels of W^{24+} accounting for the correlation, relativistic, and QED effects were performed. They demonstrated the high efficiency of the methods used. All these levels correspond to $[Kr]4d^{10}4f^4$, $[Kr]4d^{10}4f^35s$, $[Kr]4d^{10}4f^35p$, and $[Kr]4d^94f^5$ configurations. The main peculiarity of the ground configuration consists in the fact that the electron transitions in the usual form of electric-dipole radiation from the closest excited configurations to the ground configuration are strictly forbidden.

In **2012**, the results obtained in 2011 were prepared for publication. Three research papers were submitted for publication. The following investigations were also performed.

- The influence of configuration basis size on the determined results for the ground $4p^64d$ configuration and excited $4p^64f$ and $4p^54d^2$ configurations of the W^{37+} ions has been investigated. The energy levels, parameters of their wave function expansion, Lande-factors, radiative lifetimes have been calculated together with data for the electric dipole, electric quadrupole and magnetic dipole transitions inside and between the investigated configurations.
- The consideration of the average characteristics of the configuration interaction (CI) and their influence on the transition arrays and revelation of some regularities of CI manifestation in various ions of tungsten have been performed.
- The higher multipolarities of the electric transition probabilities in W^{24+} were investigated. Usually, it is accepted that the probabilities of the electric-multipole electron transitions are rapidly decreasing functions of their multipolarity. Therefore, while calculating the probabilities of electronic transitions between the configurations of certain chosen parities, it seems sufficient to take into account the first nonzero term, i.e., to consider the electron transitions of lowest multipolarity permitted by the exact selection rules. The work was aimed at verifying this assumption on the example of electric-octupole transitions in W^{24+} ion. For this purpose the large-scale multiconfiguration Hartree-Fock and Dirac-Fock calculations have been performed for the configurations $[Kr]4d^{10}4f^4$ and $[Kr]4d^{10}4f^35s$ energy levels of W^{24+} ion. The relativistic corrections were taken into account in the

quasirelativistic Breit-Pauli and fully relativistic Breit (taking into account QED effects) approximations. The role of correlation, relativistic, and QED corrections was discussed. Line strengths, oscillator strengths, and transition probabilities in Coulomb and Babushkin gauges were obtained for $E1$ and $E3$ transitions among these levels.

4.1 Investigation of spectroscopic parameters of tungsten ions

In parallel to electron-impact data calculation, we have continued studies of tungsten ions with open 4d-shell. We have investigated spectroscopic characteristics of the configurations $4p^64d^2$ and $4p^54d^3+4p^64d4f$ for the W^{36+} ion and configurations $4p^64d^3$ and $4p^54d^4+4p^64d^24f$ for W^{35+} ion applying our original quasirelativistic approach with comprehensive inclusion of correlation effects. Determined energy levels of ground configurations have demonstrated good agreement with available experimental data. Agreement with other completely relativistic calculations was good both for energy level spectra and for electron radiative transition parameters of 4d-shell. Experimental and theoretical data for the excited configurations were not available so far. But these data are important for modeling high-temperature tokamak plasma spectra. Our obtained data were submitted for publishing as 2 research papers in Atomic Data Nuclear Data Tables journal.

An important effect was discovered during investigation of spectroscopic parameters for the W^{36+} and W^{35+} ions. There are some levels of excited configurations which cannot decay to the ground configuration by way of $E1$ transitions. Such transitions are forbidden by selection rules for total momentum J . To determine radiative lifetimes for these levels, one usually computes $M1$ and $E2$ transition probabilities. As our calculations have demonstrated, this is not enough. Some of these

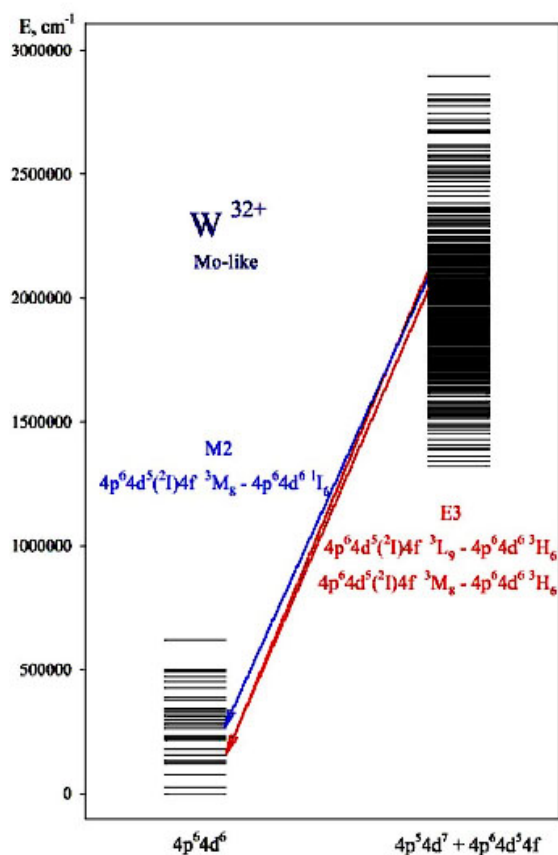


Figure 4.1 Energy levels of W^{32+} ion

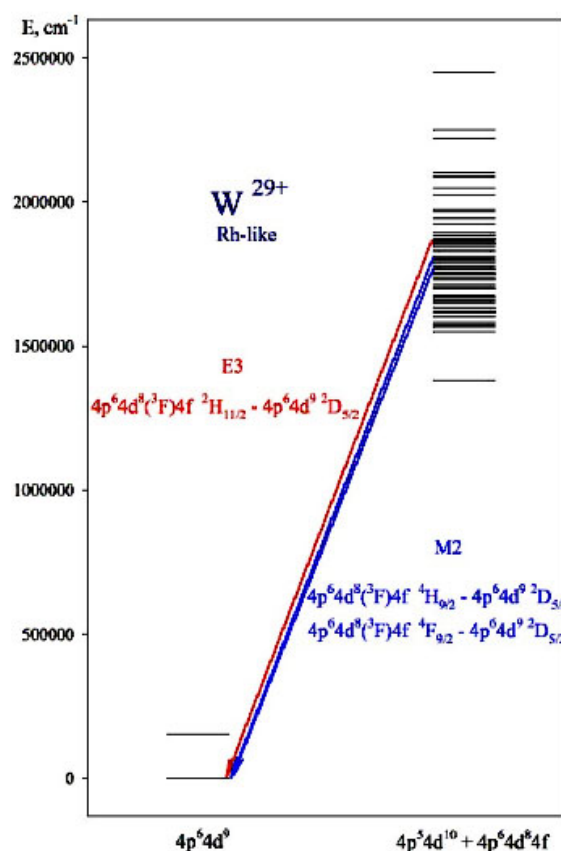


Figure 4.2 Energy levels of W^{29+} ion

levels have relatively strong M2 and E3 transitions down to the ground configuration. Inclusion of such transitions for the radiative lifetime calculations can decrease lifetime values several times or even a dozen times. Keeping that in mind, we have investigated the dependence of radiative lifetimes on M2 and E3 transition probabilities for the particular levels of $4p^5 4d^{N+1} + 4p^6 4d^{N-1} 4f$ configurations.

The investigation was carried out for four isoelectronic sequences of multicharged ions with $Z = 50-92$. Their ground configurations were $4d^2$, $4d^4$, $4d^6$ and $4d^9$. Figure 4.1 and Figure 4.2 show the energy level spectra of two tungsten ions and those M2 and E3 transitions which have a strong influence on level radiative lifetimes.

Influence of M2 and E3 transitions on level radiative lifetimes was considered by calculating parameter $R = \tau_{E2+M1} / \tau_{TOT}$. Here τ_{TOT} stands for total radiative lifetime determined by including all possible radiative transitions, and τ_{E2+M1} denotes radiative lifetime determined from the transitions among the levels of the same configuration. Our investigation has demonstrated that parameter R usually decreases when Z increases. But there can be exceptions for this rule as well, e.g. Figure 4.3 demonstrates a “non-standard” behaviour, where R initially decreases with Z increase, but later it starts to increase sharply. Such behaviour can be explained by the dependence on Z of the transition probabilities presented in Figure 4.4. It is clearly seen that the M1 transition probability initially increases and reaches its maximum value when Z increases. For higher Z -values it begins to decrease, similarly to M2 transition probabilities. Meanwhile, the transition probabilities for two E3 transitions increase steadily and become larger than those of M1 transition when $Z > 84$.

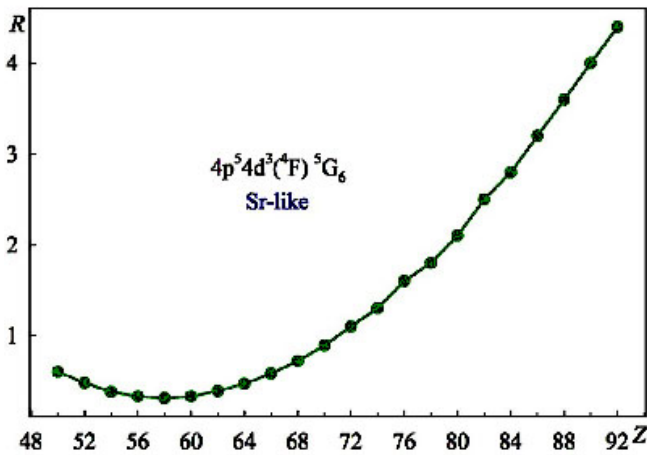


Figure 4.3
Dependence of parameter R on nuclear charge

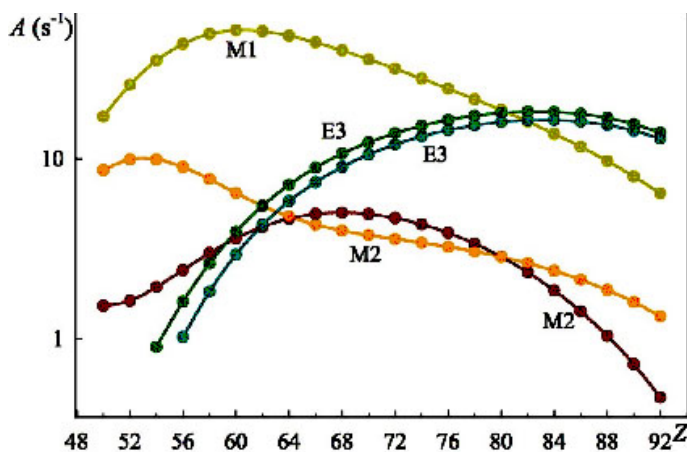


Figure 4.4
Dependence of transition probabilities from level $4p^5 4d^3 (^4F) ^5G_6$ on nuclear charge

There are some cases where dependence $R(Z)$ is non-monotonic. A sample is given in Figure 4.5. An explanation of that is provided in Figure 4.6 where a part of isoelectronic sequence dependence $A(Z)$ is demonstrated for few main transitions. It is clearly seen that transition probability for M2 transition becomes very small when $Z = 58$. Such a decrease materializes when a transition matrix element changes its sign and at some Z value becomes equal to zero. Radiative transition probability is proportional to the square of a transition matrix element. The received results were presented at ICAMDATA 2012 conference held in NIST, Gaithersburg, USA.

Figure 4.5
Dependence of parameter R on nuclear charge

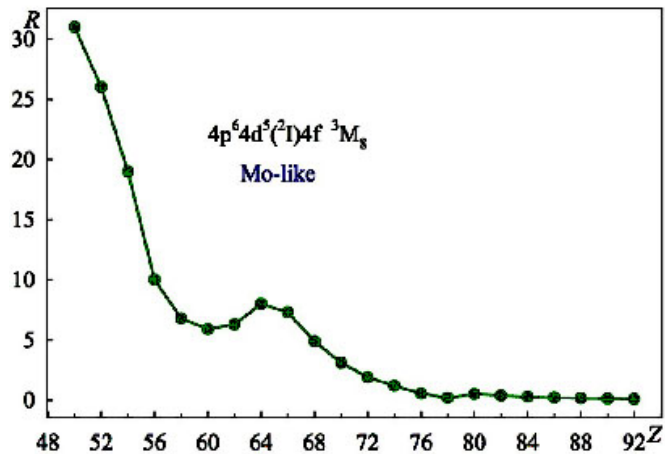
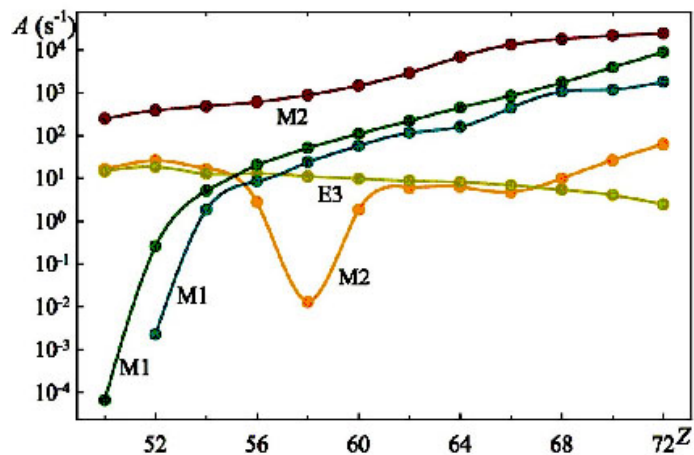


Figure 4.6
Dependence of transition probabilities from level $4p^6 4d^5 (2I) 4f^3 M_g$ on nuclear charge



4.2 New method for evaluation of the accuracy of electron transitions

Tungsten will be used as a wall material in fusion devices. Therefore, the data on spectral properties of its various ions are of great importance. Such ions, having simple electronic configurations of open shells, are studied widely both experimentally and theoretically, but this is not the case for ions, having open f-shell, due to the large number of the energy levels. The use of the second quantization method in coupled tensorial form combined with quasispin technique, described in

[4.1], opens the real possibilities to efficiently consider such configurations, as well. Indeed, the paper [4.2] supports this conclusion. Moreover, it revealed the unexpected phenomenon, stating that a large part of electric octopole (E3) transitions may be interpreted as electric dipole (E1) transitions and their probabilities on average are million times higher than those of E1 transitions.

The goal of this work was a further study of such ions by performing the large-scale multiconfiguration Dirac-Fock calculations for the lowest 30 energy levels of W^{8+} ion. We used the multiconfiguration Dirac-Fock (MCDF) approach taking into account relativistic and QED corrections [4.1]. In the multiconfiguration Dirac-Fock approximation, an atomic state function (ASF) of parity P , $\Psi(\gamma P J)$, is given by a linear combination of symmetry-adapted configuration state functions (CSFs) with the same parity, $\Phi(\gamma_i P J)$, i.e.

$$\Psi(\gamma P J) = \sum_i c_i \Phi_i(\gamma_i P J), \quad (4.1)$$

where J is the total angular momentum of the configuration. The multiconfiguration energy functional is based on the Dirac-Coulomb Hamiltonian, given by (in a.u.),

$$H_{DC} = \sum_{j=1}^N (\alpha_j \cdot \mathbf{p}_j + (\beta_j - 1)c^2 + V(r_j)) + \sum_{j < k}^N \frac{1}{r_{jk}}, \quad (4.2)$$

where α and β are the fourth-order Dirac matrices, \mathbf{p} is the momentum operator, and V is the electrostatic electron-nucleus interaction. In all the calculations reported here, the nuclear charge distribution was modelled by the two-component Fermi function.

The relativistic configuration interaction (RCI) method was used to include the transverse Breit interaction at the low-frequency limit (describing the transversely polarized photon contributions to the electron-electron interactions in Coulomb gauge), and the QED corrections (including self-energy and vacuum polarization) [4.3, 4.4]. MCDF calculations were performed with the GRASP2K [4.3, 4.5] relativistic atomic structure package in which for calculations of spin-angular parts of matrix elements the second quantization method in coupled tensorial form and quasispin technique were adopted. This allowed us to achieve the breakthrough in the field, to essentially increase the efficacy and the speed of the calculations, opening the possibilities to consider extremely complex electronic configurations.

We used a multi-reference (MR) set for the construction of the ASFs. In this approach, the configuration state functions of the multiconfigurational calculations include, in (eq. 4.1), single and double substitutions from the core 4p, 4d, 5s and valence 4f, 5p shells. Restricted active spaces of the CSFs are generated using the following AS of the orbitals:

$$\begin{aligned} AS_0 = & 1s^2 2s^2 2p^6 3s^2 3p^6 3d^{10} 4s^2 4p^6 4d^{10} 4f^{14} 5s^2 5p^4 \\ & + 1s^2 2s^2 2p^6 3s^2 3p^6 3d^{10} 4s^2 4p^6 4d^{10} 4f^{13} 5s^2 5p^5 \\ & + 1s^2 2s^2 2p^6 3s^2 3p^6 3d^{10} 4s^2 4p^6 4d^{10} 4f^{12} 5s^2 5p^6, \end{aligned}$$

$$AS_5 = AS_0 + \{5d, 5f\},$$

$$AS_6 = AS_5 + \{6s, 6p, 6d, 6f\}.$$

At all steps, only new orbitals were optimized. In order to reduce the size of the multiconfiguration expansion for $n = 5$, and $n = 6$, the jj reduction technique was applied [4.3].

Table 4.1 The lowest energy levels of W^{8+} ion in LS-coupling

No	Pos	J	Parity	Energy Total (a.u.)	Levels (cm^{-1})	Splitting (cm^{-1})	Configuration
1	1	2	+	-16111.8034658	0.00	0.00	$4f^{14}({}^1S) 1S 5s^2 5p^4({}^3P) 3P$
2	1	4	+	-16111.7670988	7981.64	7981.64	$4f^{13}({}^2F) 2F 5s^2 5p^5 3F$
3	1	3	+	-16111.7658050	8265.59	283.95	$4f^{13}({}^2F) 2F 5s^2 5p^5 1F$
4	1	5	+	-16111.7444754	12946.89	4681.30	$4f^{13}({}^2F) 2F 5s^2 5p^5 3G$
5	2	3	+	-16111.6973847	23282.10	10335.21	$4f^{13}({}^2F) 2F 5s^2 5p^5 3F$
6	2	2	+	-16111.6902635	24845.03	1562.92	$4f^{13}({}^2F) 2F 5s^2 5p^5 1D$
7	1	0	+	-16111.6787089	27380.98	2535.95	$4f^{14}({}^1S) 1S 5s^2 5p^4({}^1S) 1S$
8	3	2	+	-16111.6690170	29508.11	2127.13	$4f^{13}({}^2F) 2F 5s^2 5p^5 3D$
9	2	4	+	-16111.6382904	36251.81	6743.70	$4f^{13}({}^2F) 2F 5s^2 5p^5 3G$
10	1	1	+	-16111.6302909	38007.50	1755.69	$4f^{13}({}^2F) 2F 5s^2 5p^5 3D$
11	1	6	+	-16111.4236813	83353.07	45345.56	$4f^{12}({}^3H) 3H 5s^2 5p^6 3H$
12	2	1	+	-16111.4088998	86597.23	3244.17	$4f^{14}({}^1S) 1S 5s^2 5p^4({}^3P) 3P$
13	3	4	+	-16111.3891607	90929.46	4332.23	$4f^{12}({}^3F) 3F 5s^2 5p^6 3F$
14	4	2	+	-16111.3541062	98623.04	7693.58	$4f^{14}({}^1S) 1S 5s^2 5p^4({}^1D) 1D$
15	2	5	+	-16111.3498729	99552.12	929.09	$4f^{12}({}^3H) 3H 5s^2 5p^6 3H$
16	4	4	+	-16111.3205852	105980.05	6427.93	$4f^{12}({}^3H) 3H 5s^2 5p^6 3H$
17	3	3	+	-16111.3145253	107310.04	1329.99	$4f^{13}({}^2F) 3F 5s^2 5p^5 3D$
18	5	2	+	-16111.3076437	108820.38	1510.34	$4f^{12}({}^3F) 3F 5s^2 5p^6 3F$
19	4	3	+	-16111.3058425	109215.70	395.32	$4f^{12}({}^3F) 3F 5s^2 5p^6 3F$
20	5	4	+	-16111.2981175	110911.12	1695.42	$4f^{13}({}^2F) 2F 5s^2 5p^5 1G$
21	5	3	+	-16111.2498913	121495.56	10584.44	$4f^{13}({}^2F) 2F 5s^2 5p^5 3G$
22	6	4	+	-16111.2485029	121800.27	304.71	$4f^{12}({}^1G) 1G 5s^2 5p^6 1G$
23	6	2	+	-16111.2162142	128886.82	7086.54	$4f^{12}({}^1G) 1D 5s^2 5p^6 1D$
24	7	2	+	-16111.1919654	134208.82	5322.01	$4f^{13}({}^2F) 2F 5s^2 5p^5 3F$
25	2	0	+	-16111.1616046	140872.25	6663.43	$4f^{12}({}^3P) 3P 5s^2 5p^6 3P$
26	2	6	+	-16111.1614315	140910.25	38.00	$4f^{12}({}^1I) 1I 5s^2 5p^6 1I$
27	3	1	+	-16111.1472635	144019.75	3109.50	$4f^{12}({}^3P) 3P 5s^2 5p^6 3P$
28	8	2	+	-16111.1261035	148663.84	4644.09	$4f^{12}({}^3P) 3P 5s^2 5p^6 3P$
29	3	0	+	-16110.9461071	188168.48	39504.64	$4f^{14}({}^1S) 1S 5s^2 5p^4({}^3P) 3P$
30	4	0	+	-16110.826748	213941.90	25773.42	$4f^{12}({}^1S) 1S 5s^2 5p^6 1S$

In case of the MCDF expansions of the even ASFs for the energy spectrum calculations we used a MR set of CSFs based on the $[Kr]4d^{10}4f^{14}5s^2 5p^4$, $[Kr]4d^{10}4f^{13}5s^2 5p^5$ and $[Kr]4d^{10}4f^{12}5s^2 5p^6$ even configurations. The state functions of these three configurations form the basis for the zero-

order wave function (MR set). The energy functional on which the orbitals were optimized was defined according to an extended optimal level (EOL) scheme, where a linear combination of atomic states, corresponding to the lowest four with $J = 0$, three with $J = 1$, eight with $J = 2$, five with $J = 3$, six with $J = 4$, two with $J = 5$ and two with $J = 6$ states, were used. Admixed CSFs were obtained from single and double substitutions from some close and all open shell orbitals to an increasing active set (AS) of orbitals. Figure 4.7 displays energies of 30 lowest levels of W^{8+} belonging to $[Kr]4d^{10}4f^{14}5s^25p^4$ (5 levels), $[Kr]4d^{10}4f^{13}5s^25p^5$ (12 levels) and $[Kr]4d^{10}4f^{12}5s^25p^6$ (13 levels) configurations. Analysing the results (see Table 4.1 and Figure 4.7), we conclude that the lowest excited configurations are strongly mixed with the ground one. Therefore, here we have the unique situation, when the real electronic configuration is the linear combination of several configurations, having almost equal weights, and, thus, single-configuration approximation is absolutely unfit.

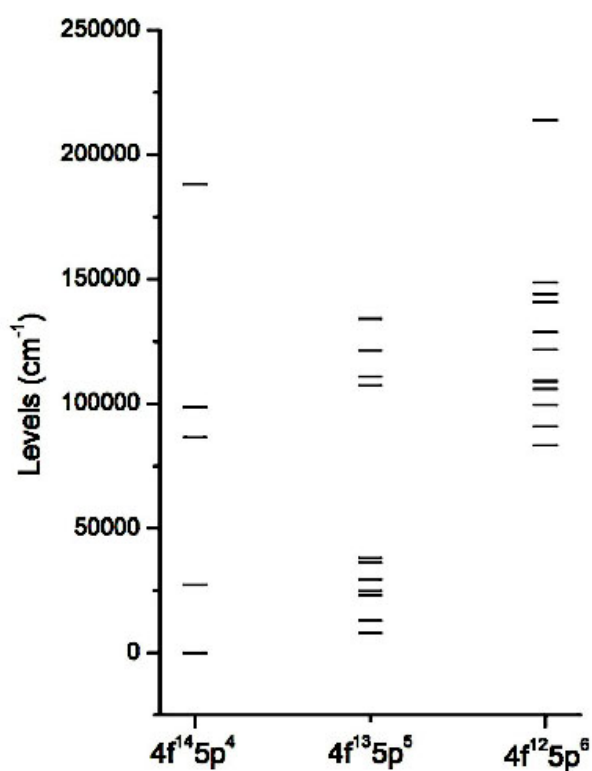


Figure 4.7
The levels of the lowest configurations of W^{8+}

Our calculations show that the ground energy level of W^{8+} ion is $[Kr]4d^{10}4f^{14}(1S)5s^25p^4(3P) 3P$ and the first excited is $[Kr]4d^{10}4f^{13}(2F)5s^25p^5 3F$ with the separation of 7981.64 cm^{-1} . In Table 4.2, the jj -coupling notation of a CSF denotes the total J for a multiply occupied shell in parentheses, whereas the resultant of coupling two subshells or, in general, a subconfiguration and a subshell, is given in square brackets. The orbital $4p_{-}$, for example, is a $4p_{1/2}$ orbital whereas $4p$ is $4p_{3/2}$. Only in five cases the component of the wave function is significantly greater in LSJ than the component in jj . In other cases, they are similar or LSJ is considerably less. A wave function or corresponding energy levels are often designed as the label of the CSF with the largest expansion coefficient. But the labels determined in this manner are not unique ones in our case. An algorithm is proposed for defining unique labels. Basically, for a given set of wave functions for the same J and parity, the CSF with largest expansion coefficient is used as the label for the function containing this largest component. Once a label is assigned, the corresponding CSF is removed from consideration in the determination of the next label. The last remaining label for a wave function may be based on a contribution that is exceedingly small as seen for the level at $128\,886.82 \text{ cm}^{-1}$ labelled in Table 4.2.

Table 4.2 The lowest energy levels and wave-function composition of of W^{8+} ion

No	Label	Pos J	Levels (cm)	Composition	
				jj coupling	LSJ coupling
1	$4f^{14}(1S) 1S 5s^2 5p^5(3P) 3P$	1 2	0.00	$88 4f^6 4f^8 5s^2 5p^2 5p^2(2)$ $+ 6 4f^6 4f^7(7/2) 5s^2 5p^2 5p^3(3/2)$	$64 + 24 (1/2D) 1D$ $+ 5 4f^{13}(2F) 2F 5s^2 5p^5 1D$
2	$4f^{13}(2F) 2F 5s^2 5p^5 3F$	1 4	7981.64	$92 4f^6 4f^7(7/2) 5s^2 5p^2 5p^3(3/2)$ $+ 3 4f^5(5/2) 4f^7 5s^2 5p^2(3/2)$	$77 + 10 1G + 9 3G$
3	$4f^{13}(2F) 2F 5s^2 5p^5 1F$	1 3	8265.59	$93 4f^6 4f^7(7/2) 5s^2 5p^2 5p^3(3/2)$ $+ 2 4f^5(5/2) 4f^8 5s^2 5p^2 5p^3(3/2)$	$56 + 27 3D + 9 3F + 4 3G$
4	$4f^{13}(2F) 2F 5s^2 5p^5 3G$	1 5	12946.89	$96 4f^6 4f^7(7/2) 5s^2 5p^2 5p^3(3/2)$	96
5	$4f^{13}(2F) 2F 5s^2 5p^5 3F$	2 3	23282.10	$93 4f^5(5/2) 4f^8 5s^2 5p^2 5p^3(3/2)$ $+ 2 4f^6 4f^7(7/2) 5s^2 5p^2 5p^3(3/2)$	$59 + 16 3G + 14 1F + 6 3D$
6	$4f^{13}(2F) 2F 5s^2 5p^5 1D$	2 2	24845.03	$82 4f^6 4f^7(7/2) 5s^2 5p^2 5p^3(3/2)$ $+ 6 4f^6 4f^8 5s^2 5p^2 5p^2(2)$ $+ 5 4f^5(5/2) 4f^8 5s^2 5p^2 5p^3(3/2)$ $+ 3 4f^6 4f^8(5s^2 5p^1(1/2) 5p^3(3/2)$	$50 + 21 3D + 17 3F$ $+ 8 4f^{14}(1S) 1S 5s^2 5p^4(3P) 3P$
7	$4f^{14}(1S) 1S 5s^2 5p^4(1S) 1S$	1 0	27380.98	$92 4f^6 4f^8 5s^2 5p^2(0)$ $+ 2 4f^6 4f^8 5s^2 5p^4$	$50 + 45 (3P) 3P$
8	$4f^{13}(2F) 2F 5s^2 5p^5 3D$	3 2	29508.11	$90 4f^5(5/2) 4f^8 5s^2 5p^2 5p^3(3/2)$ $+ 6 4f^6 4f^8 5s^2 5p^2 5p^2(2)$	$50 + 45 3F$
9	$4f^{13}(2F) 2F 5s^2 5p^5 3G$	2 4	36251.81	$92 4f^5(5/2) 4f^8 5s^2 5p^2 5p^3(3/2)$ $+ 3 4f^6 4f^7(7/2) 5s^2 5p^2 5p^3(3/2)$	$51 + 45 1G$
10	$4f^{13}(2F) 2F 5s^2 5p^5 3D$	1 1	38007.50	$96 4f^5(5/2) 4f^8 5s^2 5p^2 5p^3(3/2)$	96
11	$4f^{12}(3H) 3H 5s^2 5p^6 3H$	1 6	83353.07	$89 4f^6 4f^6 5s^2 5p^2 5p^4$ $+ 7 4f^5(5/2) 4f^7(7/2) [6] 5s^2 5p^2 5p^4$	$95 + 1 4f^{12}(1I) 1I 5s^2 5p^6 1I$
12	$4f^{14}(1S) 1S 5s^2 5p^4(3P) 3P$	2 1	86597.23	$94 4f^6 4f^8 5s^2 5p^1(1/2) 5p^3(3/2)$	94
13	$4f^{12}(3F) 3F 5s^2 5p^6 3F$	3 4	90929.46	$96 4f^6 4f^6(4) 5s^2 5p^2 5p^4$	58 $+ 32 4f^{12}(1G) 1G 5s^2 5p^6 1G$ $+ 6 4f^{12}(3H) 3H 5s^2 5p^6 3H$
14	$4f^{14}(1S) 1S 5s^2 5p^4(1D) 1D$	4 2	98623.04	$75 4f^6 4f^8 5s^2 5p^1(1/2) 5p^3(3/2)$ $+ 9 4f^5(5/2) 4f^8 5s^2 5p^1(1/2) [2] 5p^4$ $+ 6 4f^6 4f^6(2) 5s^2 5p^2 5p^4$	$56 + 19 (3P) 3P$ $+ 6 4f^{13}(2F) 2F 5s^2 5p^5 3F$ $+ 6 4f^{12}(1D) 1D 5s^2 5p^6 1D$

Table 4.2 Continued

No	Label	Pos J	Levels (cm)	Composition	
				jj coupling	LSJ coupling
14				+ 3 4f ⁵ (5/2)4f ⁷ (7/2)[2]5s ² 5p ² 5p ⁴ + 14f ⁶ 4f ⁷ (7/2)5s ² 5p ² 5p ³ (3/2)	+4 4f ¹³ (² ₁ F) ² F 5s ² 5p ⁵ ³ D +3 4f ¹² (³ ₁ F) ³ F 5s ² 5p ⁶ ³ F
15	4f ¹² (³ ₁ H) ³ H 5s ² 5p ⁶ ³ H	2 5	99552.12	96 4f ⁵ (5/2)4f ⁷ (7/2)[5]5s ² 5p ² 5p ⁴	96
16	4f ¹² (³ ₁ H) ³ H 5s ² 5p ⁶ ³ H	4 4	105980.05	85 4f ⁵ (5/2)4f ⁷ (7/2)[4]5s ² 5p ² 5p ⁴ + 7 4f ⁴ (4)4f ⁸ 5s ² 5p ² 5p ⁴ + 4 4f ⁶ 4f ⁷ (7/2)5s ² 5p ¹ (1/2)[4]5p ⁴	42 + 30 4f ¹² (³ ₁ F) ³ F 5s ² 5p ⁶ ³ F +20 4f ¹² (¹ ₁ G) ¹ G 5s ² 5p ⁶ ¹ G + 2 4f ¹³ (² ₁ F) ² F 5s ² 5p ⁵ ¹ G + 2 4f ¹³ (² ₁ F) ² F 5s ² 5p ⁵ ³ G
17	4f ¹² (² ₁ F) ² F 5s ² 5p ⁵ ³ D	3 3	107310.04	71 4f ⁶ 4f ⁷ (7/2)5s ² 5p ¹ (1/2)[3]5p ⁴ + 25 4f ⁵ (5/2)4f ⁷ (7/2)[3]5s ² 5p ² 5p ⁴	45 + 25 4f ¹² (³ ₁ F) ³ F 5s ² 5p ⁶ ³ F + 17 ³ F + 8 ¹ F + 1 ³ G
18	4f ¹² (³ ₁ F) ³ F 5s ² 5p ⁶ ³ F	5 2	108820.38	55 4f ⁶ 4f ⁶ (2)5s ² 5p ² 5p ⁴ + 22 4f ⁵ (5/2)4f ⁷ (7/2)[2]5s ² 5p ² 5p ⁴ + 11 4f ⁴ (2)4f ⁸ 5s ² 5p ² 5p ⁴ + 6 4f ⁶ 4f ⁸ 5s ² 5p ¹ (1/2)5p ³ (3/2) + 14 4f ⁵ (5/2)4f ⁸ 5s ² 5p ¹ (1/2)[2]5p ⁴	60 + 24 4f ¹² (¹ ₁ D) ¹ D 5s ² 5p ⁶ ¹ D + 5 4f ¹⁴ (¹ ₁ S) ¹ S 5s ² 5p ⁴ (¹ ₂ D) ¹ D + 4 4f ¹² (³ ₁ P) ³ P 5s ² 5p ⁶ ³ P + 1 4f ¹⁴ (¹ ₁ S) ¹ S 5s ² 5p ⁴ (³ ₂ P)
19	4f ¹² (³ ₁ F) ³ F 5s ² 5p ⁶ ³ F	4 3	109215.70	71 4f ⁵ (5/2)4f ⁷ (7/2)[3]5s ² 5p ² 5p ⁴ + 24 4f ⁶ 4f ⁷ (7/2)5s ² 5p ¹ (1/2)[3]5p ⁴	71 + 16 4f ¹³ (² ₁ F) ² F 5s ² 5p ⁵ ³ D + 6 4f ¹³ (² ₁ F) ² F 5s ² 5p ⁵ ³ F + 3 4f ¹³ (² ₁ F) ² F 5s ² 5p ⁵ ¹ F
20	4f ¹³ (² ₁ F) ² F 5s ² 5p ⁵ ³ G	5 4	110911.12	90 4f ⁶ 4f ⁷ (7/2)5s ² 5p ¹ (1/2)[4]5p ⁴ + 3 4f ⁵ (5/2)4f ⁷ (7/2)[4]5s ² 5p ² 5p ⁴ + 2 4f ⁴ (4)4f ⁸ 5s ² 5p ² 5p ⁴	39 + 34 ³ G + 18 ³ F + 4 4f ¹² (³ ₁ H) ³ H 5s ² 5p ⁶ ³ H
21	4f ¹³ (² ₁ F) ² F 5s ² 5p ⁵ ³ G	5 3	121495.56	96 4f ⁵ (5/2)4f ⁸ 5s ² 5p ¹ (1/2)[3]5p ⁴	74 + 15 ¹ F + 5 ³ F + 1 ³ D
22	4f ¹² (¹ ₁ G) ¹ G 5s ² 5p ⁶ ¹ G	6 4	121800.27	87 4f ⁴ (4)4f ⁸ 5s ² 5p ² 5p ⁴ + 8 4f ⁵ (5/2)4f ⁷ (7/2)[4]5s ² 5p ² 5p ⁴	44 + 44 4f ¹² (³ ₁ H) ³ H 5s ² 5p ⁶ ³ H + 8 4f ¹² (³ ₁ F) ³ F 5s ² 5p ⁶ ³ F
23	4f ¹² (¹ ₁ D) ¹ D 5s ² 5p ⁶ ¹ D	6 2	128886.82	30 4f ⁶ 4f ⁶ (2)5s ² 5p ² 5p ⁴ + 30 4f ⁵ (5/2)4f ⁷ (7/2)[2]5s ² 5p ² 5p ⁴ + 26 4f ⁴ (2)4f ⁸ 5s ² 5p ² 5p ⁴	26 + 36 4f ¹² (³ ₁ P) ³ P 5s ² 5p ⁶ ³ P + 25 4f ¹² (³ ₁ F) ³ F 5s ² 5p ⁶ ³ F + 4 4f ¹³ (² ₁ F) ² F 5s ² 5p ⁵ ¹ D

Table 4.2 Continued

No	Label	Pos J	Levels (cm)	Composition	
				<i>jj</i> coupling	<i>LSJ</i> coupling
				+9 $4f^5(5/2)4f^85s^25p^1(1/2)[2]5p^4$	+3 $4f^{13}({}^2F) {}^2F 5s^25p^5 {}^3F$ +2 $4f^{13}({}^2F) {}^2F 5s^25p^5 {}^3D$
24	$4f^{13}({}^2F) {}^2F 5s^25p^5 {}^3F$	7 2	134208.82	74 $4f^5(5/2)4f^85s^25p^1(1/2)[2]5p^4$ +8 $4f^64f^85s^25p^1(1/2)5p^3(3/2)$ +7 $4f^5(5/2)4f^7(7/2)[2]5s^25p^2_5p^4$ +4 $4f^64f^6(2)5s^25p^2_5p^4$	23 + 35 1D + 17 3D +10 $4f^{12}({}^3P) {}^3P 5s^25p^6 {}^3P$ +8 $4f^{14}({}^1S) {}^1S 5s^25p^4({}^1_2D) {}^1D$ +1 $4f^{14}({}^1S) {}^1S 5s^25p^4({}^3_2P) {}^3P$
25	$4f^{12}({}^3P) {}^3P 5s^25p^6 {}^3P$	2 0	140872.25	70 $4f^64f^6(0)5s^25p^2_5p^4$ +26 $4f^4(0)4f^85s^25p^2_5p^4$	87 + 9 $4f^{12}({}^1S) {}^1S 5s^25p^6 {}^1S$
26	$4f^{12}({}^1I) {}^1I 5s^25p^6 {}^1I$	2 6	140910.25	89 $4f^5(5/2)4f^7(7/2)[6]5s^25p^2_5p^4$ +7 $4f^64f^6(6)5s^25p^2_5p^4$	95 + 1 $4f^{12}({}^3H) {}^3H 5s^25p^6 {}^3H$
27	$4f^{12}({}^3P) {}^3P 5s^25p^6 {}^3P$	3 1	144019.75	95 $4f^5(5/2)4f^7(7/2)[1]5s^25p^2_5p^4$	95
28	$4f^{12}({}^3P) {}^3P 5s^25p^6 {}^3P$	8 2	148663.84	58 $4f^4(2)4f^85s^25p^2_5p^4$ +34 $4f^5(5/2)4f^7(7/2)[2]5s^25p^2_5p^4$ +2 $4f^64f^85s^25p^1(1/2)5p^3(3/2)$ +1 $4f^5(5/2)4f^85s^25p^1(1/2)[2]5p^4$	46 +40 $4f^{12}({}^1D) {}^1D 5s^25p^6 {}^1D$ +6 $4f^{12}({}^3F) {}^3F 5s^25p^6 {}^3F$ +2 $4f^{14}({}^1S) {}^1S 5s^25p^4({}^1_2D) {}^1D$
29	$4f^{14}({}^1S) {}^1S 5s^25p^4({}^3_2P) {}^3P$	3 0	188168.48	51 $4f^64f^85s^25p^2_5p^4$ +32 $4f^5(0)4f^85s^25p^2_5p^4$ +11 $4f^64f^6(0)5s^25p^2_5p^4$	30 + 39 $4f^{12}({}^1S) {}^1S 5s^25p^6 {}^1S$ +22 1S +4 $4f^{12}({}^3P) {}^3P 5s^25p^6 {}^3P$
30	$4f^{12}({}^1S) {}^1S 5s^25p^6 {}^1S$	4 0	213941.90	41 $4f^64f^85s^25p^2_5p^4$ +38 $4f^4(0)4f^85s^25p^2_5p^4$ +14 $4f^64f^6(0)5s^25p^2_5p^4$ +2 $4f^64f^85s^25p^2_5p^4$	47 +23 $4f^{14}({}^1S) {}^1S 5s^25p^4({}^1_0S) {}^1S$ +20 $4f^{14}({}^1S) {}^1S 5s^25p^4({}^3_1P) {}^3P$ +5 $4f^{12}({}^3P) {}^3P 5s^25p^6 {}^3P$

After performed work, it is concluded that with the revised GRASP2K code, it was possible to compute the energy of $4f^{14}5s^25p^4$, $4f^{13}5s^25p^5$ and $4f^{12}5s^25p^6$ levels using SD-MR method. Because the 4f and 5p subshells are unfilled, the interaction with other configurations from $n = 4$ and $n = 5$ complexes are of prime importance. The major components of the wave function were compared in *jj* and *LSJ* coupling. Although in *jj* coupling most of the expansions have a dominant component.

4.3 Theoretical calculation of dielectronic recombination coefficients for fusion plasma in relativistic approximation

The abundances derived from spectroscopic data depend critically on the accuracy of the atomic data used. Our aim is to improve the quality of existing atomic data and assess their accuracy. Ideally, one would measure abundances of all ion stages of any element. In practice, for reasons of wavelength coverage, line detectability, instrument angle etc., one often observes only a few ions. Thus, it is important to take into account ionization corrections while estimating element abundances based on a few ions or few ionization stages of the same chemical element. Ionization corrections are different for different elements, which affects conclusions based on relative abundances. However, all estimates of ionization corrections are sensitive to the adopted values of dielectronic recombination (DR) rates, which are unknown for ions of most elements in the third row of the periodic table and beyond, especially for those with high Z values. This also underscores the need for accurate recombination calculations.

DR rates are unknown for low stages of ionization of most elements in the third row of the periodic table and beyond. The situation is even more complicated for heavy atoms and ions, such as tungsten ions.

Dielectronic recombination process involves forming doubly excited (autoionizing) states that subsequently radiatively stabilize below the autoionization threshold. The total DR rate coefficient, assuming the Maxwellian distribution of the electron energy, after summing over all autoionization channels is given by formula:

$$\alpha_i^{DR}(T) = \frac{\alpha_0^3}{2g_i} \left(\frac{4\pi d_H}{k_B T} \right)^{3/2} \sum_j g_j A_{ji}^\alpha B_j \exp\left(-\frac{E_{ij}}{k_B T}\right),$$

where i is the initial state of the recombining ion, j is a doubly excited state, g_i and g_j are their statistical weights, E_{ij} is the resonance energy (the energy of continuum electron), A_{ji}^α is the autoionization rate, d_H is the Rydberg energy, k_B is the Boltzmann constant and a_0^B is the Bohr radius. The radiative stabilizing branching ratio B_j is expressed by

$$B_j = \frac{\sum_k A_{jk}'}{\sum_j A_{ji}^\alpha + \sum_s A_{js}'},$$

where A' is the radiative transition rate (probability) between two levels.

Since low temperature DR rates which are important for ionization balance studies are very sensitive to resonance energies E_{ij}' , we extend our calculations by using not only theoretical energy level data but also by introducing observed level energy values or resonance energy values to improve the accuracy of calculated DR rates. This approach allows us to remove the uncertainties of DR rates arising due to inaccurate calculated energies. For the high-temperature end, DR rates are significantly less dependent on the resonance energy accuracy.

In our investigation we have applied The Flexible Atomic Code (FAC) [4.6] to determine all basic atomic data: energy levels E_i , autoionization rates A^α , and radiative transition rates A' . These data were computed in fully relativistic approximation. Ions with electron numbers from $N_e = 15$ up to $N_e = 26$ were investigated. Electron promotions $\Delta n = 0$ and $\Delta n = 1$ were considered for autoionizing states.

Calculations were performed for tungsten ions and for the ions from the fourth row. The later case is important for two reasons. First of all, more experimental data are available for these elements,

and we can introduce energy corrections into our DR rate calculations. Secondly, it becomes possible to compare our results with other calculations, which can be performed in semirelativistic Breit-Pauli approximation. Here we (together with our colleagues from Strathclyde University, UK) utilize the `AUTOSTRUCTURE` code to calculate DR rates for selected atoms and ions. These runs will cross-check the accuracy of data generated by `FAC` code. Both `FAC` and `AUTOSTRUCTURE` codes use the independent processes, isolated resonance approximation and distorted wave function basis for the continuum electron.

In Figure 4.8 we compare our new DR rate calculation results with those obtained in previous calculation using `AUTOSTRUCTURE` code. New calculation data were obtained with an experimental energy shift. It is clearly seen that energy corrections affect very significantly DR rate values with changes reaching more than factor of 5 at low temperatures. It confirms necessity to apply highly accurate atomic data for energy levels in order to eliminate arising inaccuracies. We plan to continue investigating dielectronic recombination process for tungsten ions by introducing available high-quality energy level data.

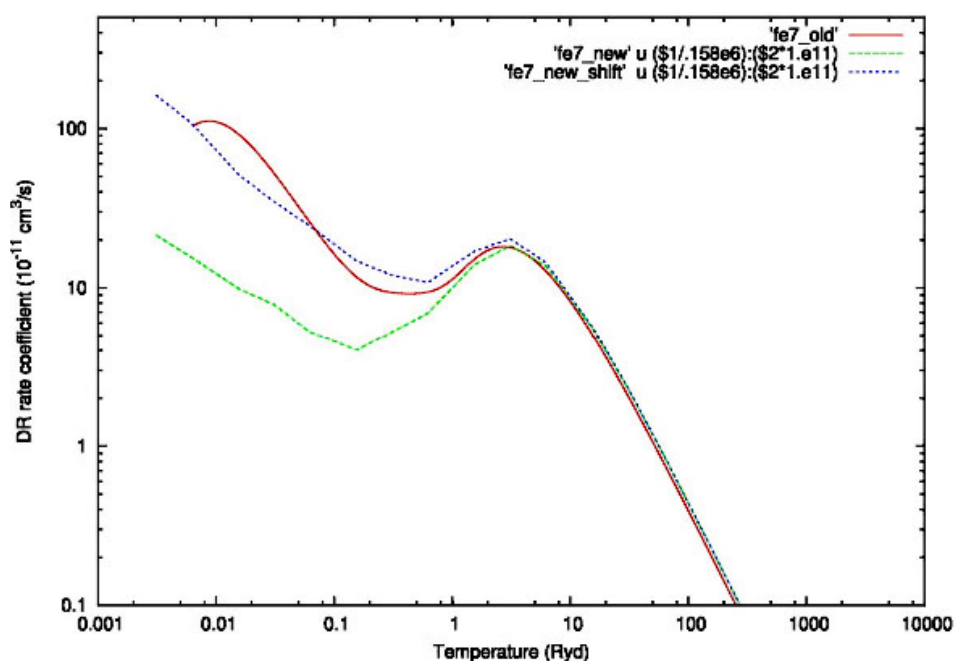


Figure 4.8
Dielectronic
recombination
rates for Fe^{6+} ions

4.4 Investigation of energy spectrum and decay probabilities in Cs atom and Cs⁻ ion

Firing beams of high-speed neutral atoms into the plasma is one of the main heating methods used in tokamaks. Traditionally, fusion machines use neutral beam systems with positive ions that are accelerated and neutralized before they enter the plasma. However, a lot of energy is lost during the neutralization process. This loss increases rapidly with the rising beam energy. A power plant requires a one MeV beam to operate, and for this the neutralization efficiency would be as low as 2%. It seems nearly impossible to attach an electron to a beam particle that is moving at some ten thousand kilometres per second. Causing the particle to lose electrons is much easier – the neutralization efficiency for a negative ion beam is 58% at the same energy level. ITER and the demonstration power plant DEMO will therefore use negative ion neutral beam systems. Europe is in charge of providing the ITER system and a test bed is under construction at Consorzio RFX, Italy [4.7].

The Beam Emission Spectroscopy system makes measurements by detecting the light emitted when neutral atoms are injected into plasmas to heat it. The diagnostics very high time resolution

allows fusion researchers to map the evolution of turbulent structures at small angles [4.8]. The injected atoms of Cs will interact with plasma particles. They will be excited and ionized increasing energy losses due to the electromagnetic radiation. Therefore, it is important to investigate atomic structure and the rates of the interaction of them with electrons, photons and deuterium ions.

Isolated negative ion of Cs is stable. The affinity of it in the ground state $5p^6s^2\ ^1S_0$ was obtained 0.08 eV. It was calculated with FAC computer code [4.6]. The transfer of Cs^- to Cs is possible in the following processes:

- ionization by electric field,
- photodetachment or photoionization,
- ionization by electrons and protons.

These processes are more effective when the atom is created in the excited states [4.9, 4.10]. Theoretical investigation of negative ions is more complicated comparing to neutral atoms and positive ions. The peculiarities of their investigation are not taken into account while the computer codes for the calculations were created. Therefore, the calculations of the decay rates of negative ions are a complicated task. One of the possibilities to investigate the negative ions is to consider them as resonances in the electron-impact excitation cross sections by using close coupling approximation [4.9, 4.11]. The knowledge of energy levels for the calculations of resonances is necessary. The classification of the energy levels of the doubly excited Cs atoms was made for the first time [4.12] by using highly accurate calculations with the help of FAC code [4.6]. The calculated excitation energies, cross sections and autoionization probabilities are presented in Table 4.3. Theoretical energies and cross sections were used for the identification of measured ejected-electron spectrum [4.13]. The autoionization rates calculated by implementing the present project enabled us to evaluate the effectiveness of the decay probabilities of the doubly excited states of Cs atoms.

Table 4.3 Calculated (E_{Cl}) and measured (E_{exp} [4.13]) excitation energies in eV, excitation cross sections (in 10^{-18} cm²) and autoionization probabilities for Cs $5p^5nln'l'$ LSJ states

No. [13]	LSJ	E_{Cl}	A^a	Excitation cross sections for 0.07; 1.05; 5; 10 and 50 eV of ejected electrons	E_{exp} [4.13]
1	$6s^2\ ^2P_{3/2}$	12.310	1.26+13	29.76, 18.41, 24.02, 25.82, 12.04	12.307
2	$5d(^3P)6s\ ^4P_{1/2}$	12.737	4.93+11	14.00, 3.87, 2.26, 0.92, 0.16	12.786
3	$5d(^3P)6s\ ^4P_{3/2}$	12.905	1.34+11	26.48, 9.19, 7.42, 5.44, 2.06	12.930
4	$6s(^3P)6p\ ^4S_{3/2}$	13.148	1.02+09	15.58, 2.50, 0.69, 0.35, 0.05	13.011
5	$5d(^3P)6s\ ^4P_{5/2}$	13.168	5.61+09	31.84, 8.76, 4.73, 1.75, 0.23	13.149
6	$5d(^3P)6s\ ^2P_{1/2}$	13.197	3.52+13	14.52, 4.98, 4.40, 3.36, 1.49	13.204
	$5d(^3F)6s\ ^4F_{9/2}$	13.230	9.45+01	27.99, 8.18, 3.41, 1.13, 0.15	
7	$5d(^3F)6s\ ^4F_{7/2}$	13.402	6.69+10	20.46, 7.62, 4.28, 2.62, 0.86	13.344
8	$6s(^3P)6p\ ^4D_{7/2}$	13.495	1.36+07	8.99, 1.79, 0.52, 0.21, 0.03	13.484
9	$6s(^3P)6p\ ^4D_{5/2}$	13.539	5.77+11	6.53, 2.79, 1.90, 1.64, 0.66	13.526
10	$5d(^3F)6s\ ^4F_{5/2}$	13.584	9.42+10	13.74, 6.13, 4.01, 2.91, 1.07	13.600
11	$6s(^1P)6p\ ^2D_{3/2}$	13.650	3.65+11	3.98, 2.18, 1.66, 1.50, 0.61	13.651
12	$5d(^3F)6s\ ^2F_{7/2}$	13.718	1.05+13	17.48, 5.70, 2.80, 1.41, 0.40	13.689
13	$5d(^3P)6s\ ^2P_{3/2}$	13.718	1.34+13	13.79, 6.52, 6.87, 6.52, 2.93	13.756
14	$5d(^3F)6s\ ^4F_{3/2}$	13.797	6.12+11	7.34, 2.60, 1.85, 1.50, 0.63	13.825
15	$6s(^1P)6p\ ^2P_{1/2}$	13.811	1.05+11	1.68, 1.00, 0.50, 0.40, 0.16	13.952

Table 4.3 Continued

No. [13]	LSJ	E_{ci}	A^a	Excitation cross sections for 0.07; 1.05; 5; 10 and 50 eV of ejected electrons	E_{exp} [4.13]
16	5d(¹ D)6s ² D _{5/2}	13.817	4.15+12	8.87, 3.31, 1.00, 1.25, 0.44	14.043
	5d(³ D)6s ⁴ D _{7/2}	13.888	2.98+12	9.14, 8.37, 7.49, 6.84, 2.83	
	6s(³ P)6p ⁴ P _{5/2}	13.971	4.34+11	4.14, 2.33, 1.78, 1.71, 0.73	
	6s(¹ P)6p ⁴ D _{3/2}	13.994	1.04+10	2.94, 1.79, 1.41, 1.34, 0.57	
	6s(¹ P)6p ² S _{1/2}	14.005	7.71+10	5.70, 4.43, 3.84, 3.43, 1.40	
	5d(³ D)6s ² D _{5/2}	14.013	1.06+12	5.78, 5.97, 3.16, 2.52, 0.93	
17	5d ² (³ F) ⁴ D _{1/2}	14.069	7.15+12	4.84, 5.18, 8.13, 9.27, 4.40	14.072
18	6s(³ P)6p ⁴ P _{1/2}	14.198	1.50+12	2.38, 4.10, 2.36, 1.98, 0.77	14.208
19	5d ² (³ F) ⁴ D _{3/2}	14.213	4.48+12	4.29, 2.73, 3.39, 3.62, 1.70	14.310
	6s(³ P)6p ² P _{3/2}	14.240	3.10+11	1.16, 1.11, 0.97, 0.96, 0.42	
20	6s(³ P)6p ² D _{5/2}	14.337	3.80+12	1.89, 1.25, 1.00, 0.95, 0.41	14.427
	5d ² (³ F) ² D _{5/2}	14.372	8.50+10	3.34, 3.10, 2.80, 2.26, 1.07	
21	6s ² (¹ S) ² P _{1/2}	14.498	2.85+12	4.84, 3.24, 4.40, 5.21, 2.66	14.480
22	5d ² (³ F) ⁴ D _{7/2}	14.567	3.70+11	3.30, 2.86, 2.55, 2.31, 0.97	14.519
23	5d(³ P)6p ⁴ P _{1/2}	14.572	5.07+12	3.76, 8.41, 5.08, 4.50, 1.90	
	5d(³ P)6p ⁴ D _{5/2}	14.615	9.34+11	1.65, 0.61, 0.37, 0.31, 0.12	
	5d(³ P)6p ² P _{1/2}	14.654	7.50+10	3.02, 5.97, 3.50, 3.02, 1.24	14.574
24	5d ² (³ P) ² P _{3/2}	14.809	2.50+13	2.34, 0.81, 0.52, 0.35, 0.13	14.704
	5d ² (³ P) ⁴ P _{5/2}	14.817	3.00+11	2.26, 0.60, 0.31, 0.14, 0.03	
25	5d(¹ P)6s ² P _{1/2}	14.855	2.93+13	9.91, 11.68, 18.72, 21.91, 10.89	14.893
	5d ² (¹ G) ² F _{5/2}	14.872	4.91+12	2.28, 0.68, 0.29, 0.10, 0.02	
25	5d(³ D)6s ² D _{3/2}	14.886	8.83+12	25.81, 29.16, 46.40, 54.13, 26.9	14.893
26	5d(³ P)6p ⁴ P _{5/2}	14.897	1.80+11	0.51, 0.10, 0.02, 0.01, 0.00	14.950
27	6s(³ P)6p ² S _{1/2}	14.997	1.34+13	2.43, 4.81, 3.10, 2.71, 1.07	15.055
	5d ² (³ P) ⁴ P _{3/2}	15.040	6.29+12	4.16, 4.05, 6.31, 7.32, 3.66	
	6s(³ P)7s ⁴ P _{5/2}	15.130	3.34+09	4.59, 0.87, 0.30, 0.11, 0.02	
	5d ² (³ P) ⁴ P _{1/2}	15.145	1.26+10	1.91, 1.72, 2.60, 2.97, 1.46	
28	5d(¹ D)6p ² D _{3/2}	15.178	1.26+10	0.50, 0.30, 0.26, 0.24, 0.10	15.111
29	6s(³ P)7s ⁴ P _{3/2}	15.209	1.42+12	2.51, 1.89, 2.97, 3.37, 1.68	15.171
	5d ² (¹ D) ² P _{1/2}	15.224	1.60+12	1.23, 0.63, 0.65, 0.68, 0.31	
	5d ² (¹ D) ² D _{5/2}	15.235	2.03+12	2.70, 0.95, 0.48, 0.28, 0.09	
30	5d(³ D)6p ⁴ P _{3/2}	15.239	2.18+10	0.37, 0.08, 0.03, 0.02, 0.01	15.211
31	5d ² (¹ D) ² F _{7/2}	15.246	7.69+11	0.45, 0.14, 0.06, 0.03, 0.01	15.314
32	5d(³ F)6p ⁴ F _{7/2}	15.274	2.16+11	0.02, 0.01, 0.00, 0.00, 0.00	15.375
	5d(³ P)6p ² S _{1/2}	15.286	6.32+10	2.03, 5.01, 2.84, 2.41, 1.01	
33	6s(³ P)7s ² P _{3/2}	15.289	1.02+12	2.48, 1.83, 2.66, 2.95, 1.44	15.399
33	5d ² (³ P) ⁴ S _{3/2}	15.378	2.56+12	2.44, 1.42, 1.66, 1.77, 0.85	15.399
	5d ² (³ P) ⁴ D _{7/2}	15.449	1.63+11	2.50, 1.13, 0.74, 0.55, 0.22	
	5d(³ F)6s ⁴ F _{3/2}	15.478	8.27+10	5.52, 1.78, 0.88, 0.48, 0.16	
34	5d(³ P)6s ⁴ P _{5/2}	15.490	4.99+11	7.50, 2.69, 1.40, 0.77, 0.23	15.486
	6s(³ P)7p ⁴ S _{3/2}	15.519	1.68+11	1.48, 0.25, 0.07, 0.04, 0.01	

Table 4.3 Continued

<i>No.</i> <i>[13]</i>	<i>LSJ</i>	<i>E_C</i>	<i>A^a</i>	<i>Excitation cross sections for 0.07; 1.05; 5; 10 and 50 eV of ejected electrons</i>	<i>E_{exp}</i> <i>[4.13]</i>
35	5d(³ F)6s ² F _{5/2}	15.534	1.36+12	5.38, 1.81, 0.81, 0.37, 0.09	15.521
36	5d ² (³ F) ⁴ F _{3/2}	15.556	1.06+12	1.79, 0.58, 0.27, 0.18, 0.02	15.572
	6s(³ F)6d ⁴ F _{7/2}	15.622	4.95+10	2.01, 1.27, 0.97, 0.81, 0.33	
37	6s(³ P)6d ⁴ F _{9/2}	15.648	1.55+10	1.06, 0.36, 0.15, 0.05, 0.01	
	6s(³ P)6d ² F _{7/2}	15.654	2.69+11	1.98, 0.61, 0.25, 0.11, 0.03	
	6s(³ P)6d ⁴ D _{5/2}	15.656	2.00+10	1.27, 0.43, 0.20, 0.11, 0.04	
	6s(³ P)6d ² D _{5/2}	15.667	9.11+09	2.59, 1.28, 0.89, 0.70, 0.29	15.655
	5d(³ P)6d ⁴ F _{5/2}	15.711	2.16+12	1.29, 0.40, 0.16, 0.06, 0.01	
39	5d(³ P)6d ⁴ F _{7/2}	15.734	2.68+11	2.31, 2.28, 2.14, 1.99, 0.88	15.742
	5d(³ F)6s ⁴ F _{7/2}	15.755	3.21+07	4.26, 4.08, 3.80, 3.52, 1.55	
	5d(³ P)6d ⁴ F _{3/2}	15.757	1.80+10	1.20, 0.74, 0.95, 1.5, 0.53	
	6s(³ P)6p ⁴ D _{3/2}	15.760	1.61+12	1.35, 0.51, 0.32, 0.28, 0.20	
40	5d(³ F)6s ² F _{5/2}	15.810	8.17+12	4.17, 2.87, 2.40, 2.11, 0.91	15.801
	6s(¹ P)7s ² P _{3/2}	15.824	6.85+12	0.87, 0.69, 0.95, 0.99, 0.45	
	6s(¹ P)6p ² D _{5/2}	15.842	1.19+12	2.04, 1.95, 1.67, 1.65, 0.74	15.853
	6s(³ P)6p ⁴ P _{3/2}	15.843	1.60+06	2.94, 0.59, 0.17, 0.08, 0.01	
	6s(³ P)7s ² P _{1/2}	15.849	2.42+12	1.05, 1.36, 2.44, 3.01, 1.61	
	5d ² (³ P) ² D _{3/2}	15.910	1.32+12	1.16, 0.41, 0.23, 0.13, 0.04	
42	6s(³ P)7p ⁴ D _{5/2}	15.950	1.10+13	1.42, 0.75, 0.55, 0.54, 0.24	15.922
	5d ² (¹ S) ² P _{3/2}	15.938	2.45+12	1.89, 1.95, 3.22, 3.76, 1.92	15.996
	5d ² (³ F) ² D _{5/2}	15.943	4.79+11	1.27, 0.59, 0.42, 0.35, 0.15	
	6s(³ P)8s ⁴ P _{5/2}	15.964	1.78+11	1.49, 0.51, 0.27, 0.21, 0.08	
45	6s(¹ P)6p ² S _{1/2}	16.021	2.36+12	3.95, 7.87, 4.60, 3.95, 1.60	16.177
46	6s(¹ P)6d ² P _{3/2}	16.220	3.00+12	3.08, 2.97, 4.62, 5.54, 2.94	16.270
48	5d(³ D)7p ² P _{1/2}	16.506	8.23+10	0.68, 1.80, 1.03, 0.86, 0.34	16.389
51	5d(¹ F)6d ² P _{1/2}	16.711	4.92+12	1.03, 1.23, 2.10, 2.53, 1.32	16.610
56	5d(¹ D)7p ² P _{1/2}	16.836	1.80+09	0.63, 1.95, 1.17, 1.04, 0.46	16.806
58	5d(¹ D)8s ² D _{3/2}	16.912	2.00+12	0.80, 0.95, 1.55, 1.91, 1.00	16.968
	6s(³ P)7s ⁴ P _{1/2}	17.320	3.90+09	0.60, 0.24, 0.27, 0.31, 0.17	
62	6s(¹ P)7s ² P _{3/2}	17.413	2.22+11	4.53, 7.17, 9.40, 11.70, 6.41	17.148
63	5d(³ P)7s ² S _{1/2}	17.531	4.72+12	1.97, 2.38, 4.10, 5.11, 2.78	17.186
	5d(³ P)6p ² S _{1/2}	17.571	4.41+12	1.70, 5.26, 3.08, 2.58, 1.04	17.360
	5d ² (¹ S) ² P _{1/2}	17.753	3.70+12	1.19, 1.43, 2.46, 3.08, 1.66	
	6s(³ P)6d ⁴ F _{3/2}	17.815	1.76+12	2.09, 2.04, 3.14, 3.91, 2.12	
	6s(¹ P)6d ² P _{1/2}	17.817	2.63+11	2.07, 2.42, 4.09, 5.18, 2.87	
	6s(³ P)7p ⁴ D _{1/2}	17.822	8.51+12	1.14, 3.38, 2.12, 2.07, 1.08	
	6s(³ P)6d ⁴ F _{3/2}	17.895	5.46+11	1.27, 0.97, 1.33, 1.59, 0.85	
	6s(³ P)6d ⁴ D _{1/2}	17.905	9.30+11	1.40, 1.55, 2.51, 3.16, 1.73	
	5d(³ F)7s ⁴ F _{3/2}	18.010	9.99+09	0.62, 0.72, 1.20, 1.50, 0.82	
	5d(³ D)6d ⁴ D _{1/2}	18.027	3.38+12	0.90, 1.05, 1.76, 2.20, 1.20	
	6s(³ P)7p ⁴ P _{1/2}	18.029	7.63+12	1.57, 4.98, 2.97, 2.57, 1.09	
	6s(¹ P)7p ² P _{1/2}	18.059	1.16+13	3.92, 12.95, 7.59, 6.40, 2.65	

4.5 References for Chapter 4

- 4.1. Z.R. Rudzikas. Theoretical Atomic Spectroscopy. Cambridge University Press, 2nd ed. 2007.
- 4.2. G. Gaigalas, Z. Rudzikas, P. Rynkun and A. Alkauskas. Phys. Rev. A, **83**, 032509 (2011).
- 4.3. P. Jonsson, X. He, C. Froese Fischer, and I.P. Grant. Comput. Phys. Commun., **177**, 597 (2007).
- 4.4. B. J. McKenzie, I. P. Grant, P. H. Norrington. Comput. Phys. Commun., **21**, 233 (1980).
- 4.5. C. Froese Fischer, G. Gaigalas, Y. Ralchenko. Comput. Phys. Commun., **175**, 738 (2006).
- 4.6. F. M. Gu. Flexible Atomic Code, <http://kipac-tree-stanford.edu/fac>.
- 4.7. <http://www.efda.org/newsletter/efficient-high-power-plasma-heating/>
- 4.8. Nick Hollpway. MAST reaps the benefits of international collaboration, Fusion in Europe, No. 1, 5 (2012)
- 4.9. J. Slater, F. H. Read, S. E. Novik and W. C. Lineberg. Alkali negative ions: III. Multichannel photodetachment study of Cs⁻ and K⁻. Phys. Rev. A, **17**, 201 (1978).
- 4.10. A. R. Johnston and P. D. Burrow. Temporary negative-ion states of Na, K, Rb and Cs. Phys. Rev. A, **59**, 406 (1995).
- 4.11. A. A. Borovik, O. Zatsarinny and K. Bartchat. Resonance effects in electron and photon impact excitation of the p₆ subvalence subshell in alkali atoms. J. Phys. B, **42**, 044010 (2009).
- 4.12. A. Kupliauskienė. Theoretical study of the 5p5nln'l' autoionizing states of Cs, Physica Scripta, **84**, 045304 (7pp) (2011).
- 4.13. V. Pejcev and K. J. Ross. J. Phys. B: At. Mol. Phys., **10**, 2935 (1977).

5 MOBILITY PROGRAM 2012

Plasma diagnostics:

Mr. G. Stankūnas visited CCFE on 6-9 March 2012 to discuss the work to be implemented in 2012. A visit to facility JET was performed to see the current status of the JET facility. Together with dr. S. Conroy and dr. B. Syme the cooperation activities in 2012 and plans were discussed. CAD drawings of the shield structure and material composition were collected to start the calculations.

On 11-14 December 2012 Mr. G. Stankūnas again visited Close Support Unit – Culham (CCFE) to discuss the results of performed calculations. He presented neutron calculations that have been carried out to evaluate the dose rate leakage from the shields which contain the neutron source.

Fusion safety issues:

During 2-8 December 2012, four representatives of LEI (Mr. T. Kaliatka, Mr. T. Kačegavičius, Mr. R. Karalevičius, and Mr. E. Urbonavičius) visited IPP-Griefswald, Germany to discuss the achieved results and future activities related to W7-X. A visit to facility W7-X was performed to see the current status of the W7-X facility. Together with Mr. Naujoks the co-operation activities in 2012 and plans for 2013 were discussed.

The results of LOCA analysis and assessment of Plasma Vessel venting systems were discussed. The performed analysis showed that the water hammer in the cooling circuit in case of LOCA is not expected, taking into account the realistic valve closure speed. The capacity of PV venting systems is enough to prevent overpressure in case of 40 mm pipe rupture inside PV during “baking” mode operation. The results were confirmed with two computer codes RELAP5 and COCOSYS.

The analysis of W7-X plasma vessel port AEU30 welds was performed for 1 mm and 6 mm thick weld and different welding quality. The performed analysis showed that limit loads are in comfortable distance from expected normal operation conditions, which means that safety of the welds is ensured.

As well the possible places for pipe whip and introductory pipe whip analysis was performed to investigate possibilities of such analysis.

Missions related with PPP&T implementation:

Mr. R. Alzbutas and Mr. R. Voronov participated in kick-off meetings of EFDA PPP&T agreement WP12-DTM02 that were held on 17-19 April 2012 and in the final meetings of this task that were held on 11-13 December 2012. Both meetings were held at IPP-Garching, Germany. At the kick-off meeting detailed plans for implementation of the tasks were agreed, while the final meetings were held to discuss the achieved results.

Mr. G. Stankūnas participated at EFDA PPP&T Task planning meetings on WP13-SYS02 and WP13-SYS04 that were held on 7-8 November 2012. During meetings the detailed work programs for 2013 were discussed and meeting participants were invited to submit their proposals for project calls when they become open on ECOM portal.

Meetings under EFDA:

Mr. E. Urbonavičius of LEI participated in the EFDA Public Information Network Annual Meeting, which was held in Culham (UK) on June 14-15, 2012. At EFDA Public Information Group (renamed to Public Information Network) annual meeting various public information and communication activities, including best practises, of EFDA member organisations were presented. A visit to JET facility was arranged. As well meetings of the internal working groups were held to discuss details of the issues related to public information of fusion research and how these issues could be overcome.

6 OTHER ACTIVITIES IN MAGNETIC CONFINEMENT FUSION

In collaboration with Strathclyde University researchers working on ADAS-EU project, the investigations of W ions were carried out by VU ITPA scientists. The theoretical study in quarelativistic approximation with correlation effects included in multiconfiguration approximation with transformed radial orbitals base was performed not only for four low-ionization tungsten ions ($W^{2+} - W^{5+}$), but also for adjoined element ions of hafnium ($Hf - Hf^{3+}$), tantalum ($Ta^{1+} - Ta^{4+}$) and rhenium ($Re^{3+} - Re^{6+}$).

All investigated ions have open 5d-shell in their ground configurations. It is well known that 5d-electrons have energy values close to those of 6s-electrons for neutral atoms and first ions. Since these electrons (5d and 6s) have the same parity, a strong mixing of the $5d^N$, $5d^{N-1}6s$ and $5d^{N-2}6s^2$ takes place. Therefore, the energy levels of these configurations cannot be investigated separately. Configuration mixing effects lead to a situation that the analysis of eigen-functions sometimes cannot provide a definitive assignment of particular energy level to any single above-mentioned configuration. Similar situation occurs for the excited odd configurations of these ions.

Keeping that in mind, we have chosen such an approach. The energy levels of three even-parity configurations $5d^N + 5d^{N-1}6s + 5d^{N-2}6s^2$ ($N = 1,2,3,4$) were computed simultaneously. The most important admixed configurations were selected for each of these configurations. The same approach was applied for determining energy levels of three odd-parity configurations $5d^{N-1}6p + 5d^{N-2}6s6p + 5d^{N-3}6s^26p$ ($N = 1,2,3,4$). For adjustment of admixed configurations, the basis of transformed radial orbitals with principal quantum number n in range from 7 to 9 and all possible values of orbital quantum number l was established. The selection criteria for the admixed configurations had a range from 10^{-5} to 10^{-7} . A comparatively large value (10^{-5}) for selection criteria was chosen for the configurations with $N = 4$. Nevertheless, the main correlation effects were taken into account. A simultaneous computing of three strongly-mixing configurations enabled inclusion of 3-electron and 4-electron correlation effects. The increase of value for selection criteria was caused by fact that configuration groups with $N = 4$ have huge number of LS -terms; therefore, it was not possible to extend configuration basis due to limited resources of our computer clusters. Even use of such a restricted configuration basis would consume some 400–500 CPU hours to complete calculations for one ion.

We have determined eigenvalues and eigenfunctions for the even-parity configurations $5d^N + 5d^{N-1}6s + 5d^{N-2}6s^2$ ($N = 1,2,3,4$) and the odd-parity configurations $5d^{N-1}6p + 5d^{N-2}6s6p + 5d^{N-3}6s^26p$ ($N = 1,2,3,4$) in our calculations. Applying these results, we have determined the first Born – electron-impact excitation cross sections and collision strengths for the transitions among levels of even-parity configurations and for the transitions from the levels of even-parity configurations to the levels of odd-parity configurations. Our data were transferred to the Strathclyde University collaborators.

7 PUBLIC INFORMATION

The information related to FUSION energy perspectives, last achievements in ITER **Exhibitions and communication to public**

The information related to FUSION energy perspectives, last achievements in ITER development and other Fusion research fields is continuously distributed among universities, R&D institutions, schools:

- 21 March 2012. "Career days 2012" at Kaunas University of Technology, Kaunas Lithuania. Distribution of information and discussions on FUSION to students. (<http://www.lei.lt/main.php?m=476&l=1716&k=1>)
- 24-25 May 2012. 9th Conference of young scientists on energy issues CYSENI 2012 (www.cyseni.com). In the conference "Fusion energy" topic is included (1 of 11). No paper on fusion. (<http://www.lei.lt/main.php?m=476&l=1774&k=1>)
- Fusion activities are indicated in "Annual report 2012" of Lithuanian Energy Institute (in Lithuanian and English). Reports are distributed to energy-related companies in Lithuania and abroad, associations, ministries, Lithuanian and foreign embassies, various entities. Reports are distributed at conferences, trade shows, during the visits to the Lithuanian Energy Institute.
- Presentation in Lithuanian Academy of Sciences by Algirdas Kaliatka on 11 December 2012 on fusion in a discussion "Energy issues and future energy" (<http://naujienos.vu.lt/ivykiai/anonsai/25828-diskusija-fizikins-energetikos-problemos-ir-ateities-energetika>). Information about this presentation was published by Ugnė Karaliūnaitė and Vaidas Neverauskas in the most popular news portal DELFI: archive <http://verslas.delfi.lt/archive/article.php?id=60216115>

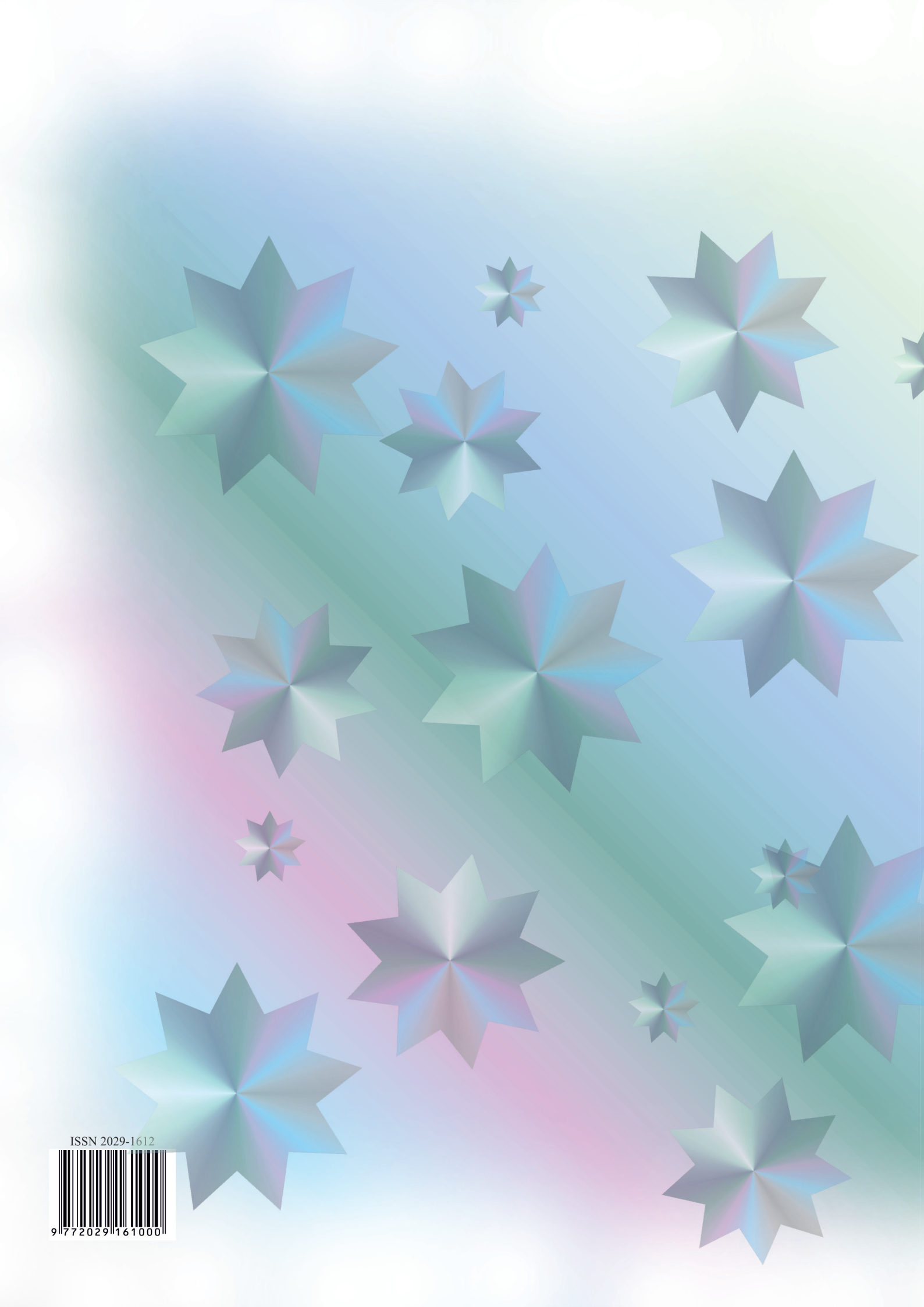
The information related to FUSION energy perspectives, last achievements in ITER development and other Fusion research fields is continuously distributed among universities, R&D institutions, schools:

- Material on fusion is provided to Kaunas University of Technology, Vilnius University and Vytautas Magnus University.
- Agency of Science, Innovation and Technology (<http://www.mita.lt>), which is responsible for co-ordination of FP7, Eureka and other international programmes activities in Lithuania is provided with the material. During other event at the Agency, participants can familiarise with the material.

Information on FUSION and EURATOM/LEI activities is placed on the web-site of Lithuanian Energy Institute <http://www.lei.lt> in section "International projects" -> "EURATOM-LEI".

8 PUBLICATIONS

- 8.1. V. Jonauskas, G. Gaigalas, S. Kučas. Relativistic calculations for M1-type transitions in $4d^N$ concentrations of $W^{29+} - W^{37+}$ ions. *Atomic Data and Nuclear Data Tables*, 98, 19-42 (2012).
- 8.2. G. Gaigalas, P. Rynkun, A. Alkauskas, Z. R. Rudzikas. The energy levels and radiative transition probabilities for electric quadrupole and magnetic dipole transitions among the levels of the ground configuration, $[KR]4d^{10}4f^4$, of W^{24+} . *Atomic Data and Nuclear Data Tables*, 98, 391-436 (2012).
- 8.3. P. Bogdanovich, R. Kisielius. Theoretical energy level spectra and transition data for $4p^64d$, $4p^64f$ and $4p^54d^2$ configurations of W^{37+} ion. *Atomic Data and Nuclear Data Tables*, 98, 557-565 (2012).
- 8.4. P. Bogdanovich, R. Karpuškieñė, R. Kisielius. Role of M2 and E2 transitions for $4p^54d^{N+1}$ and $4p^64d^{N-1}4f$ configurations level lifetimes. Abstracts of 8th ICAMDATA, NIST, Gaithersburg, USA, 2012, p. 57.
- 8.5. A. Kaliatka, E. Ušpuras, T. Kaliatka. Pressure surge in Wendelstein 7-X experimental stellarator facility. *Kerntechnik*. ISSN 0932-3902. 2012. Vol. 77, No. 2, p. 134-140.
- 8.6. T. Kaliatka, M. Povilaitis, A. Kaliatka, Urbonavičius E. Simulation of targets feeding pipe rupture in Wendelstein 7-X facility using RELAP5 and COCOSYS codes. *Journal of Fusion Energy*. ISSN 0164-0313. 2012. Vol. 31, No. 5, p. 506-517.



ISSN 2029-1612



9 772029 161000